DEVELOPMENT OF HYBRID ATOMISTIC/EMPIRICAL MODELING METHODS FOR DONOR-BASED QUANTUM COMPUTING ARCHITECTURES

A Dissertation

Submitted to the Faculty

of

Purdue University

by

Yui-Hong Matthias Tan

In Partial Fulfillment of the

Requirements for the Degree

of

Doctor of Philosophy

July 2015

Purdue University

West Lafayette, Indiana

ACKNOWLEDGMENTS

First and foremost, I would like to express my sincere gratitude to my advisor Professor Dr. Gerhard Klimeck, who has supported me throughout my graduate studies at Purdue University. This work would not have been possible without his guidance, mentorship and encouragement. I would also like to express my gratitude to Professor Dr. Ulrich Kunze at Ruhr-University Bochum, who has been a valuable mentor to me since the beginning of my studies in Germany. I would like to thank Professor Michelle Y. Simmons, Professor Supriyo Datta, Professor Alejandro Strachan and Professor Rajib Rahman for serving on my Advisory Committee and their excellent leadership. I would like to express my gratitude to Dr. Hoon Ryu (Korea Institute of Science and Technology Information) and Dr. Sunhee Lee (Samsung Advanced Institute of Technology) whose friendship and mentorship since the beginning of my PhD has led to continued research collaborations until today. I would like to thank Dr. Bent Weber (Monash University) who has been a great research collaborator and friend to me. It was a long journey towards the success of the double donor-dot project, but a great experience shaped by joint hard work, mutual encouragement and shared excitement.

This work has been supported financially by the U.S. National Science Foundation Graduate Research Fellowship Program (NSF GRFP), the Australian Research Council Centre of Excellence for Quantum Computation and Communication Technology and the U.S. Army Research Office. Computational resources on nanoHUB.org, funded by the NSF, were used extensively.

TABLE OF CONTENTS

Page

Page

LIST OF TABLES

LIST OF FIGURES

Figure Page

Figure Page

ABSTRACT

Tan, Yui-Hong Matthias Ph.D., Purdue University, July 2015. Development of Hybrid Atomistic/Empirical Modeling Methods for Donor-Based Quantum Computing Architectures. Major Professor: Gerhard Klimeck.

Silicon phosphorous donor based devices have emerged as promising candidates for future quantum computing devices. Despite the development of high precision fabrication techniques, inherent statistical variations of dopant placement on an atomic scale can influence device behavior in donor-based quantum computing systems considerably. Understanding the impact of statistical dopant placement variations on an atomic scale is thus of crucial importance for comprehensive device characterization. Existing atomistic based models such as tight-binding (TB) are to date unable to comprehensively model realistic statistical dopant placement variations in donor-based quantum computing systems due to immense computational requirements. The absence of feasible modeling methods therefore poses a significant challenge towards the goal of scalable donor-based quantum computing. Addressing the innovation imperative for novel atomic-scale methods capable of modeling realistic statistical dopant placement variations will close a major gap in current device characterization capabilities and provide important design guideline implications for future quantum computing devices. This work presents the development of novel hybrid modeling methods for single and multi-donor based quantum computing architectures. Firstly, a detailed study of the impact of lead dopant placement fluctuations in a single atom transistor is presented. Using a combined modeling approach of TB models and rate-equations, lead doping induced density of states fluctuations and their impact on the experimental charge stability diagram are investigated with atomic scale resolution. Secondly, a hybrid modeling methodology for multi-donor based quantum computing

devices is presented. Based on atomistic TB simulations, empirical models and combinatorial algorithms, this new model served instrumental in the first demonstration of Pauli spin blockade in a multi-donor based device - a milestone in the development of donor-based quantum computing technology. In detail, the hybrid model determined the exact number of donors in the experimental device by rapid computation of statistically weighted binding energy spectra comprising millions of unique possible donor configurations. Practically unfeasible with any existing methods, the presented hybrid atomistic/empirical modeling methodology facilitates, for the first time, comprehensive characterization of statistical dopant placement variation effects in donor-based quantum computing architectures with atomic scale accuracy and unprecedented speed.

1. INTRODUCTION

1.1 Preface

Quantum computing has developed from a visionary idea into one of the most fascinating areas of modern nanotechnology. The successful development of quantum computers would mark a scientific and technological milestone of extraordinary importance. Quantum computers would exponentially outperform current CMOS-based computers in terms of both speed and memory storage capabilities, thus impacting modern society immensely. In specific, silicon phosphorous donor based devices are seen as promising candidates for the realization of qubits, the quantum analogue of the bit and the fundamental building block of a future quantum computer. Donor based devices in silicon can have extremely long spin-coherence and spin-relaxation times, and would be capable of being integrated within the existing CMOS technology infrastructure. [9] The ability to control matter with atomic scale accuracy is central to the development of solid-state quantum computing architectures. Necessary atomic precision control of phosphorous dopant placement in silicon has been demonstrated using a combined fabrication method of scanning tunneling microscopy and molecular beam epitaxy. This led to recent breakthroughs in donor-based quantum computing technology including the development of a deterministic single atom transistor [9] and the first demonstration of Pauli spin blockade in a multi-donor based system [1].

1.2 Status Quo of Modeling Methods in Quantum Computing

Despite the development of high precision fabrication techniques, atomic scale statistical variations of dopant placement are inherently present. Understanding and modeling the impact of atomic scale statistical dopant placement variations in quan-

tum computing devices is of crucial importance. The atomic scale dimensions of modern quantum computing architectures necessitate modeling methods with atomistic resolution. For example, even dopant placement variations of a few angstroms can change binding energies of multi-donor quantum dots considerably [1]. Atomistic based models such as tight-binding (TB) and density functional theory (DFT) have been applied in numerous theoretical studies on donor-based quantum computing architectures [3] [4]. Modeling of realistic devices using atomistic methods often necessitates significant computational resources and access to supercomputers. Computational constraints of atomistic methods currently prohibit comprehensive modeling of statistical dopant placement variations present in realistic quantum computing architectures. The number of possible donor configurations in few multi-donor quantum dots can quickly grow into the millions, rendering comprehensive analysis of dopant placement fluctuations with current atomistic methods virtually impossible. In atomic scale devices such as donor-based quantum computing devices, inherent statistical variations of dopant placement on an atomic scale can influence device behavior considerably. The absence of feasible modeling methods therefore poses a significant unsolved challenge towards the goal of predictive and comprehensive large-scale modeling of donor-based quantum computing architectures. Understanding the impact of statistical dopant placement variations on an atomic scale is thus of crucial importance towards the development of donor-based quantum computing devices. Realistic modeling of dopant placement fluctuations on an atomic scale will enhance the accuracy and depth of current device characterization capabilities, as well as provide and challenge design guidelines implications for future quantum computing devices.

1.3 Addressing the Innovation Imperative for New Modeling Methods

This work presents the development of novel hybrid modeling methods for single and multi-donor based quantum computing architectures. In the first chapter, a detailed study of the impact of lead dopant placement fluctuations in a single atom

transistor is presented. Using a combined tight-binding/rate-equations approach the charge stability diagram of single atom transistor is reconstructed. Density of states (DOS) fluctuations in the atomic-scale phosphorus doped device leads and their impact on the charge stability diagram are modeled through multi-million atom tight binding simulations. The precise placement of the donors in the device leads substantially impacts the DOS fluctuation signatures in the charge stability diagram, thus highlighting pronounced dopant placement fluctuations effects in the single atom transistor device. The second chapter expands the discussion to multi-donor based quantum computing architectures. In specific, a hybrid modeling methodology for multi-donor based quantum computing devices is presented. Based on atomistic TB simulations, empirical models and combinatorial algorithms, this new model served instrumental in the first demonstration of Pauli spin blockade in a multi-donor based device - a milestone in the development of donor-based quantum computing technology [1]. In detail, the hybrid model determined the exact number of donors in the experimental device by rapid computation of statistically weighted binding energy spectra comprising millions of unique possible donor configurations. Practically infeasible with any existing methods, the presented hybrid atomistic/empirical modeling methodology facilitates, for the first time, comprehensive characterization of statistical dopant placement variation effects in future donor-based quantum computing devices with atomic scale accuracy and unprecedented speed. The third chapter presents proposed future work projects which build upon and expand the scope of the hybrid atomistic/empirical modeling methodology. The overarching goal is the development of a comprehensive and expandable set of hybrid empirical/atomistic models which allow high-speed and large-scale statistical device characterization of donor-based quantum computing architectures. The anticipated outcomes of the future work proposal will provide design guidelines for optimal donor cluster geometries, enable quantitative analysis of donor diffusion effects and rapid large-scale computation of key device performance indicators such has binding energies, spin relaxation times and hyperfine coupling strengths. A three stages project plan to build the foundation

of a comprehensive large-scale device characterization tool for donor-based quantum computing devices is outlined and presented in detail.

2. COULOMB BLOCKADE AND LEAD DOPANT PLACEMENT FLUCTUATIONS IN A SINGLE ATOM TRANSISTOR

2.1 Abstract

This chapter presents a detailed study of the impact of lead dopant placement fluctuations in a deterministic single atom transistor. Using a combined modeling approach of TB models and rate-equations, lead doping induced density of states fluctuations and their impact on the experimental charge stability diagram are modeled with atomic scale resolution. Random dopant placement fluctuations in the device's leads can be probed via modeling of the experimental charge stability diagrams. The precise placement of the donors in the device leads substantially impacts the DOS fluctuation signatures in the charge stability diagram, thus highlighting pronounced atomic granularity effects in the single atom transistor device. Furthermore, the experimentally observed asymmetric coupling of the source and drain device leads to the single channel phosphorus dopant is investigated and compared to experimental conditions.

2.2 Motivation

As modern semiconductor devices usher towards few nanometer length scales, atomic precision in fabrication technology is becoming increasingly important. Novel atomic-scale semiconductor devices will exhibit atomic granularity effects, where device characteristics are influenced by the specific placement of individual dopant atoms. Interface roughness, randomness in alloy and doping compositions, or strain effects will also continue to be further impacted by the atomic resolution type nature

of ultra-scaled device [2, 5–8]. Accurate dopant placement is thus crucial for studying and understanding the impact of atomic granularity effects on device behavior. Precise control of donor incorporation also constitutes a significant step towards the realization of donor-based quantum computers [20–24]. Recently, Füchsle [9] demonstrated the first single-atom transistor in which an individual phosphorus dopant atom has been deterministically placed within an epitaxial silicon device architecture. Using a combined approach of hydrogen-resist lithography and scanning tunneling microscopy, the single phosphorus dopant was positioned with a remarkably high spatial atomic level accuracy of one lattice site [9]. The source and drain leads and two in-plane gates of the device were formed with heavily phosphorus doped delta-layer wires, which can provide Ohmic conductance to the central device under atomistic control [15]. The wires also modulate the electrostatic environment of the single dopant and can control the 0, 1 and 2 electron states. Despite the presence of the highly doped leads, the silicon encapsulated single dopant retains discrete quantum states and a bulk-like charging energy; findings of important relevance for the development of future scalable atomic-scale silicon device architectures [9]. The theoretical work of Hoon et.al. [9] confirmed the existence of the single atom transistor with high confidence. Hoon et.al. not only theoretically model the charging energy and device gate controllability in excellent agreement with experiment, but also quantitatively explain the larger extent of the D- region in the charge stability diagram [9]. This work aims to further expand the theoretical modeling work of the single atom transistor. In particular, we investigate the impact of impurity placement fluctuations in the Si:P leads on the single atom transistor's charge stability diagram.

2.3 Experimental Structure, Coulomb Diamond features

Figure 1a) shows a schematic of the experimental planar single atom transistor device. A single phosphorus dopant atom is placed in the channel region between highly phosphorus doped source (S), drain (D) and gate leads (G1, G2) in a silicon

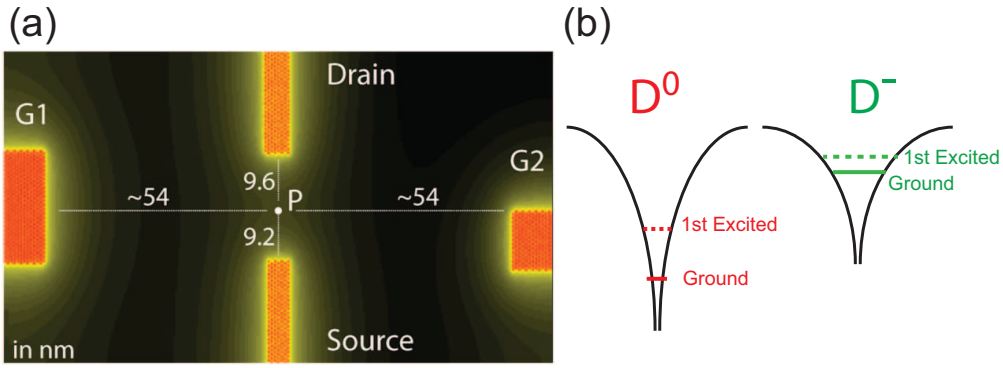

Fig. 2.1. (a) Atomistically calculated potential profile of the close-up inner Single Atom Transistor device area. The co-planar leads consist of highly phosphorus-doped monatomic layers. The white dot marker indicates the position of the single isolated phosphorus atom in the central device channel region. (b) Schematic donor potential of a single phosphorus atom in the one-electron D^0 and two-electron D^- state.

substrate environment. The gate leads are $\sim$ 54nm away from the central P donor. The source and drain leads are $\sim$ 9nm apart from the single P dopant in the channel. The gates electrostatically tune the energy states of the channel P dopant into and out of the Fermi window spanned by the voltage across the source and drain leads, thus effectively controlling current flow through the device. The leads have a universal phosphorus doping concentration of 1/4 monolayers; i.e. 1 in every 4 atoms in an atomic plane is a phosphorus (P) dopant. The ohmic conductance of these ultra-scaled nanowires has been measured [15] and modeled in detail [25]. Phosphor placement variations with the nanowire region as well as small phosphor density variations do not affect the wire conductance strongly. However we will show here that the detailed wire configurations do affect some details of the transport through the single impurity device. In fact one can argue that the single impurity states can perform a spectral analysis of the detail in the leads.

Figure 1b) shows the Coulombic potential of the single phosphorus channel dopant in the D^0 and D^- charging state. The single phosphorus donor ground state and first

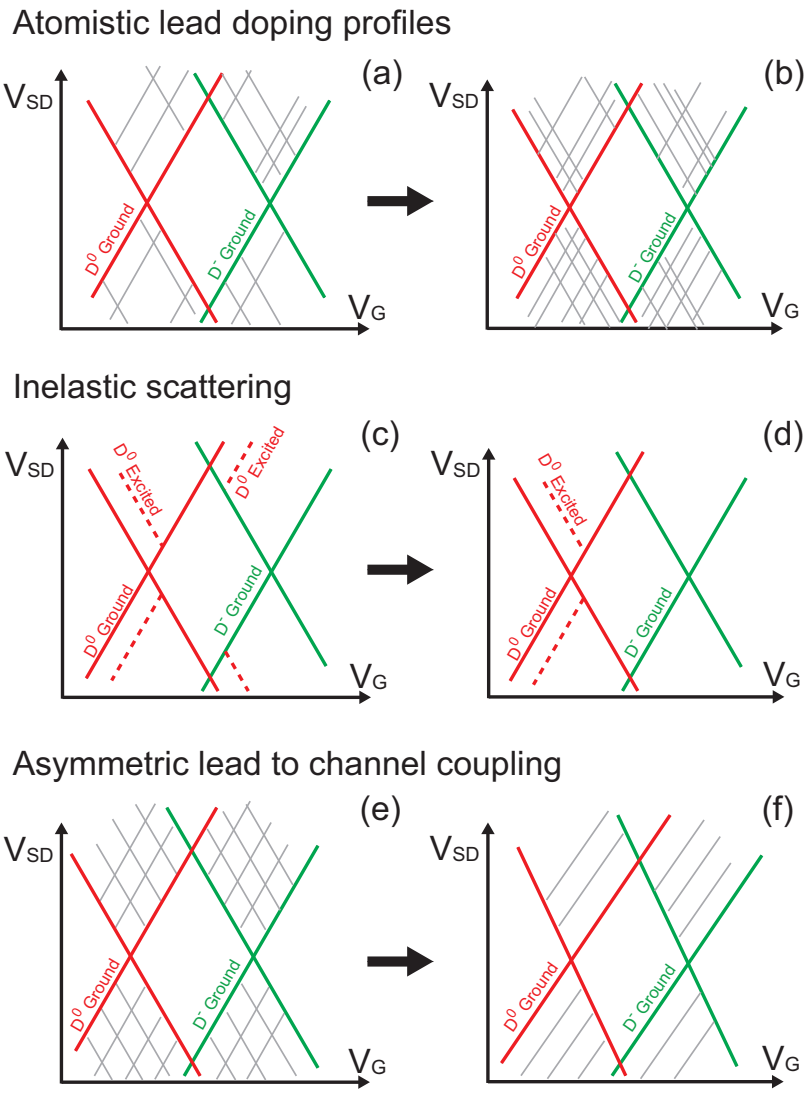

Fig. 2.2. Investigated charge stability diagram features of the single atom transistor. (a,b) Schematic charge stability diagrams with two different atomistic lead doping profiles. Conductance streaks (grey) indicate density of states fluctuations in the source/drain leads and are dependent on the atomistic doping profile of the leads. Schematic conductance streaks without (c) and with (d) inelastic scattering. Schematic conductance streaks with symmetric (c) and asymmetric (d) lead to channel donor coupling.

excited energy states are included in the subsequent modeling analysis and denoted here with solid and dashed lines, respectively. The potential profile and eigenstates

of the single phosphorus dopant were obtained through atomistic tight-binding calculations and validated against experimental data [**?**, 10, 11].

Figure 2) provides a conceptual overview of the charge stability diagram phenomena to be investigated in this work. In the first part, the impact of atomistic lead doping profiles on the charge stability diagram of the single atom transistor is investigated (Figures 2a, 2b). In the second part, inelastic scattering effects are modeled and discussed. (Figures 2c, 2d) In the third part, we conclude with modeling the asymmetric lead to channel donor coupling as observed in the experimental device. (Figures 2e, 2f)

2.4 Lead DOS fluctuations

Figure 3) shows three sample simulation unit cells for the planar delta-doped Si:P source (S) and drain (D) device leads. The doping concentration is kept close to experimental measurements at 1/4 ML, whereas the specific dopant placement differs among the three samples. As the physical length of the source and drain leads is considerably larger the leads' widths, periodic boundary conditions along the 110 direction are assumed in the modeling analysis. The center figures show the simulated density of states profiles for the three leads along the y-confinement direction as obtained through atomistic tight-binding simulations.

The Fermi level is 79 meV below the silicon bulk conduction band edge, which serves as a general energy reference in this work. To incorporate the information of the atomistically simulated lead density of states profiles into the rate-equation model [19] for simulating the charge stability diagrams, the coupling strength of the source and drain lead to the center dopant is approximated to be proportional to the energy dependent lead density of states. The right insets show the resulting charge stability diagrams with incorporation of the atomistically calculated density of states fluctuations in the device leads. Although the doping concentration and physical dimensions of the wires are identical across the three samples, the different

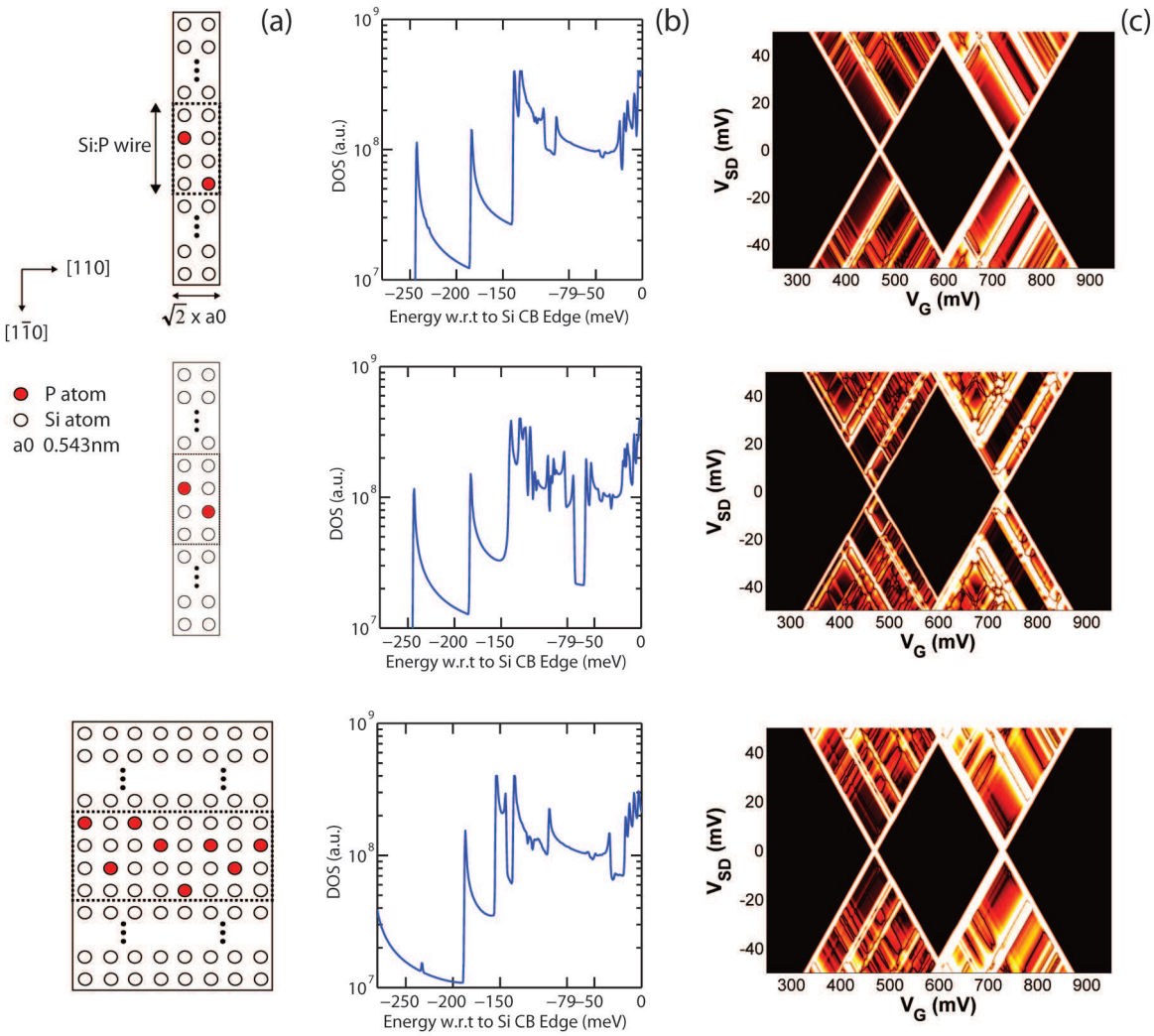

Fig. 2.3. (a) Schematic of three different Si:P device lead simulation supercells with distinct atomistic phosphorus (P) doping profiles. (b) Density of States (DOS) profiles of source and drain leads. (c) Charge Stability Diagrams (Coulomb Diamonds) showing the impact of different atomistic doping profiles.

atomic dopant profiles translate into starkly varying density of states and conductance streak patterns in the charge stability diagram. The results and theoretical charge stability diagrams indicate atomic granularity effects in the single atom transistor and highlight observable effects of individual dopant placement on device characteristics

in ultra-scaled atomic devices. One can also argue that the single impurity in the central device acts as a spectral analysis filter that measures the density of states in the leads [26, 27].

2.5 Inelastic scattering

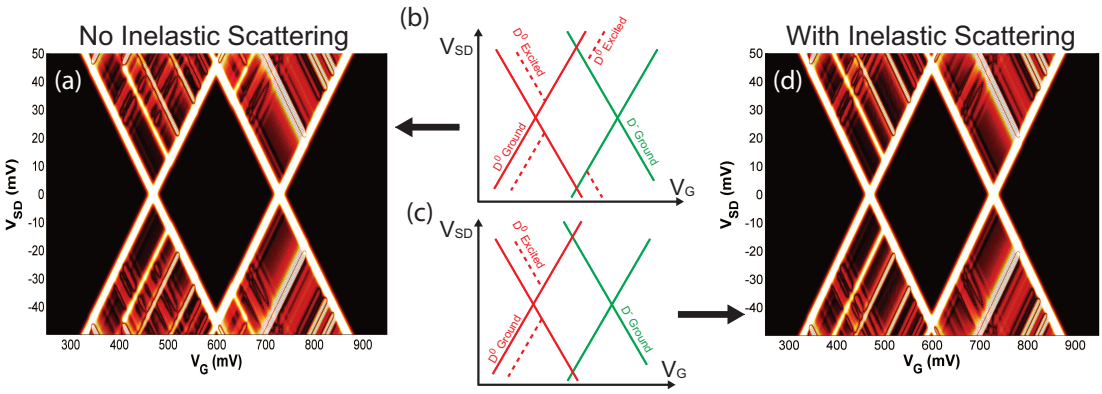

Fig. 2.4. Modeling of the impact of scattering on spectral features. (a) Completely coherent transport without incoherent scattering inside the single impurity state. (b) Schematic conductance streaks in the presence of a single excited state in the quantum dot. Streaks in the 1 electron occupation regime as indicated by "1" are labeled differently in blue. (c) Schematic conductance streaks in the presence of very strong inelastic scattering inside the QD. Streaks in the "1" electron regime disappear, due to the immediate filling of the lower state. (d) Modeled conductance spectrum under the assumption of strong inelastic scattering.

In Figure 4, the impact of inelastic scattering on the charge stability diagram characteristics of the single atom transistor is investigated. Inelastic scattering causes electrons in the excited states to relax into the energetically lower lying ground state, thus opening additional current transport paths. Due to the immediate filling of the lower ground state in the strong inelastic scattering case, conductance streaks in the "1" electron regime disappear (see Figure 4c).

2.6 Asymmetric Coupling

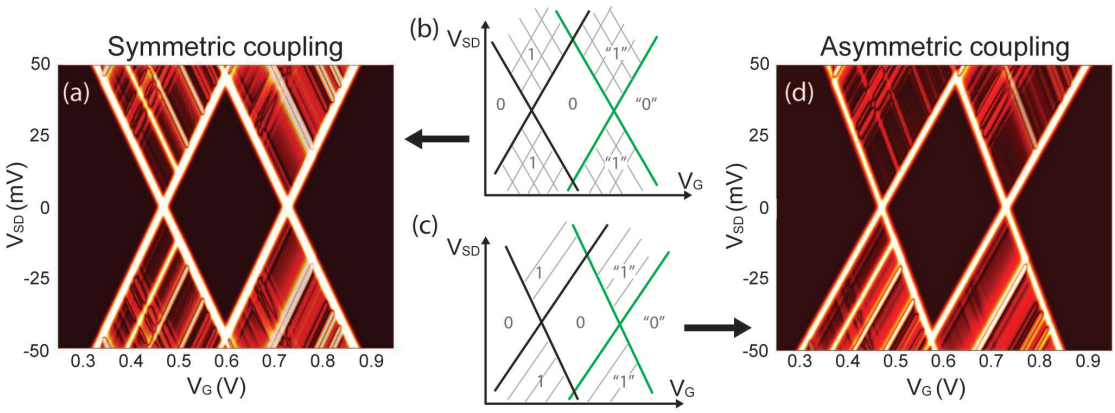

Fig. 2.5. Modeling of the impact of asymmetric lead to channel donor coupling. (a) Modeled conductance spectrum with symmetric lead to channel donor coupling. (b) Schematic conductance streaks in the presence of symmetric source/drain to channel donor coupling. Grey lines in the 1 electron occupation regimes indicate lead density of states fluctuation signatures. (c) Schematic conductance streaks in the presence of asymmetric lead to channel donor coupling with $\Gamma_{Source} << \Gamma_{Drain}$. (d) Modeled conductance spectrum with asymmetric lead to channel donor coupling.

Figure 5a) shows a modeled charge stability diagram assuming both source and drain lead are equally strongly coupled to the single dopant in the channel. The resulting DOS fluctuation signatures exhibit a symmetric streak pattern with negative and positive slope streaks along the Vg axis. Figure 5d), in contrast, depicts a theoretical charge stability diagram modeled with anti-symmetric source and drain coupling to the single dopant in the channel. By gradually reducing the coupling strength of the channel to the source with respect to the drain, we observe that the atomistic DOS fluctuation streak pattern increasingly resembles the experimentally observed charge stability diagram. The lead density of states fluctuation signatures visible in the charge stability diagram thus not only highlight atomic granularity and specific dopant placement effects, but also further confirm and characterize the

asymmetric lead device characteristics of the single atom transistor device. The slight vertical tilt of the asymmetric charge stability diagram can be stem due to asymmetric control strengths of the source and drain leads on the channel dopant, as well as due to calibration of the experimental measurement devices.

2.7 Match with Experiments

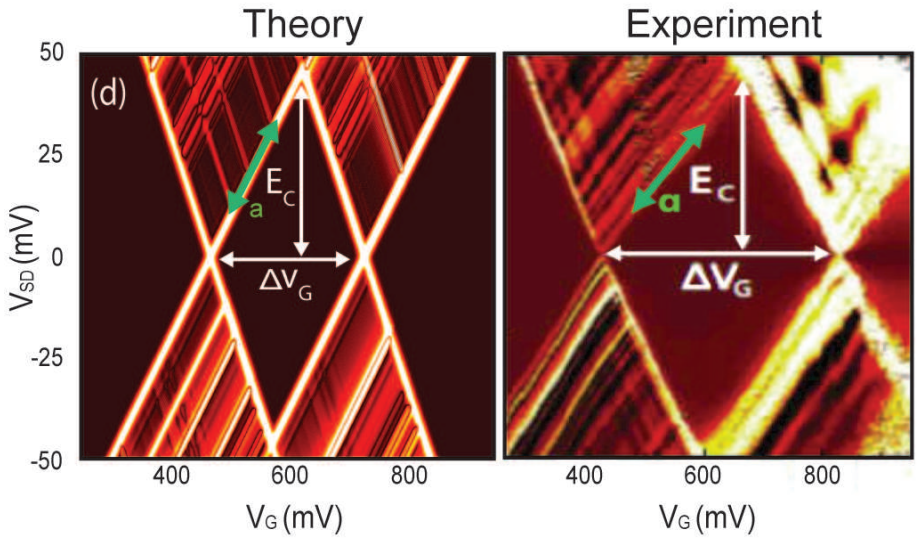

Fig. 2.6. Comparison of modeled charge stability diagram with experimental single atom transistor charge stability diagram.

Figure 6) Comparison with experiments. Detailed discussion to be adapted from Hoon's single donor modeling paper

2.8 Conclusions

Using a hybrid modeling approach combining both rate-equations and multi-million atomistic device calculations, we theoretically investigated the charge stability diagram of the world's first deterministic single atom transistor. Inelastic scattering effects and asymmetric coupling of the source/drain leads to the single channel im-

purity were theoretically modeled and compared with experimental results. We show that atomistic phosphorus dopant placement fluctuations in the leads can be probed via modeling of the experimental charge stability diagrams. Conductance streaks due to lead density of states fluctuations highlight that the exact position of dopants affects device behavior characteristics in atomic-scale devices.

3. A HYBRID ATOMISTIC/EMPIRICAL MODELING METHOD FOR DONOR-BASED QUANTUM COMPUTING DEVICES

3.1 Abstract

This chapter presents the development of a hybrid modeling methodology for multi-donor based quantum computing architectures. Based on atomistic TB simulations, empirical models and combinatorial algorithms, this new model served instrumental in the demonstration of Pauli spin blockade and exchange interaction in an experimental multi-donor based device - a milestone in the development of donor-based quantum computing technology. In detail, the hybrid model determined the exact number of donors in the experimental device by rapid computation of statistically weighted binding energy spectra comprising millions of unique possible donor configurations. Furthermore, a discussion on the experimental impact of this work, i.e. the observation of Pauli spin blockade and exchange interaction in a donor-based device, is presented.

3.2 Motivation

Electron spins confined to phosphorus donors in silicon are promising candidates as qubits1 due to their extremely long coherence times, exceeding seconds in isotopically purified bulk silicon [29]. With the recent demonstrations of initialisation, read-out, [30] and coherent manipulation [31] of individual donor electron spins, the next challenge towards the realisation of a Si:P donorbased quantum computer is the demonstration of exchange coupling [20,32,33] in two tunnel-coupled P donors. Spin-to-charge conversion [30,34] via Pauli spin-blockade [35,36] an essential ingredient for

reading out individual spin states, is challenging in donor based systems due to the inherently large donor charging energies ($\sim$ 45 meV), requiring large electric fields ($>$ 1 MV/m) to transfer both electron spins onto the same donor [37].

This work highlights the results of a double donor-dot device in which we directly observed spin-blockade of the first few electrons and measured the effective exchange interaction between electron spins in coupled Coulomb-confined systems. Careful characterization of the double-donor device using a novel hybrid atomistic/empirical modeling methodology identified the double donor-dot device as a 2P/3P system with great accuracy. Practically unfeasible with any existing methods, the hybrid atomistic/empirical modeling methodology also facilitated, for the first time, comprehensive characterization of statistical dopant placement variation effects in donor-based quantum computing architectures with atomic scale accuracy and unprecedented speed.

3.3 Modeling Methodology Examined

3.3.1 Overview of Modules

The hybrid modeling methodology was developed using a modular approach. Every module in the presented version serves as an integral part towards the goal of rapid computation of multi-million donor configuration binding energy spectra. Using a segmented framework structure allows easier debugging and faster development of additional modules and features in future versions. Figure 3.1 shows a graphical representation of the atomistic/empirical modeling framework. Currently, the hybrid modeling methodology consists of four modules, which combined together enable rapid computation of statistically weighted binding energy confidence bands. In the following sections, the different modules' functionality and objectives are explained in detail.

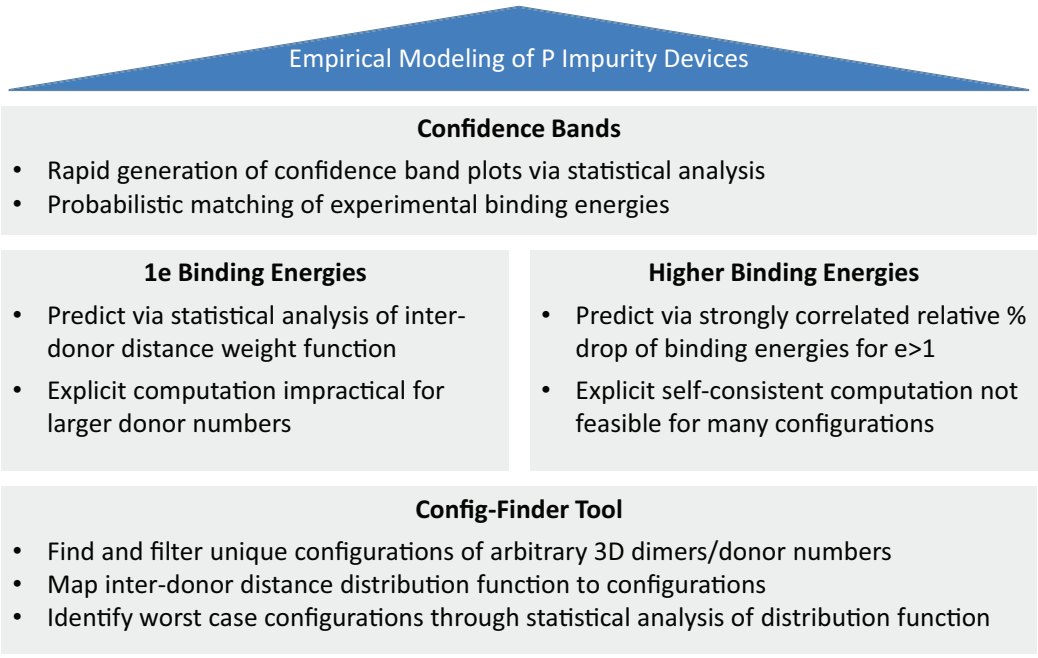

Fig. 3.1. Framework structure of hybrid atomistic/empirical modeling methodology for rapid computation of multi-million donor configuration binding energy confidence bands.

3.3.2 Configuration Finder Tool

An important question in multi-donor based quantum dot modeling is determining the number of possible donor configurations within the spatial confinement region of the quantum dot. The exact location of each donor in the quantum dot can have profound influence on the device characteristics. For example, donor placement variations of even a few angstroms have shown to alter binding energies of multi-donor quantum dots considerably. Here, we determine the number of possible donor configurations in an experimental double donor-dot device. Figure 3.2 shows the experimental double donor-dot device and STM images of the two donor-based quantum dots D1 and D2.

The configuration finder module computes the number of possible donor configurations for arbitrary 3D dimers/quantum dot dimensions and donor numbers. The

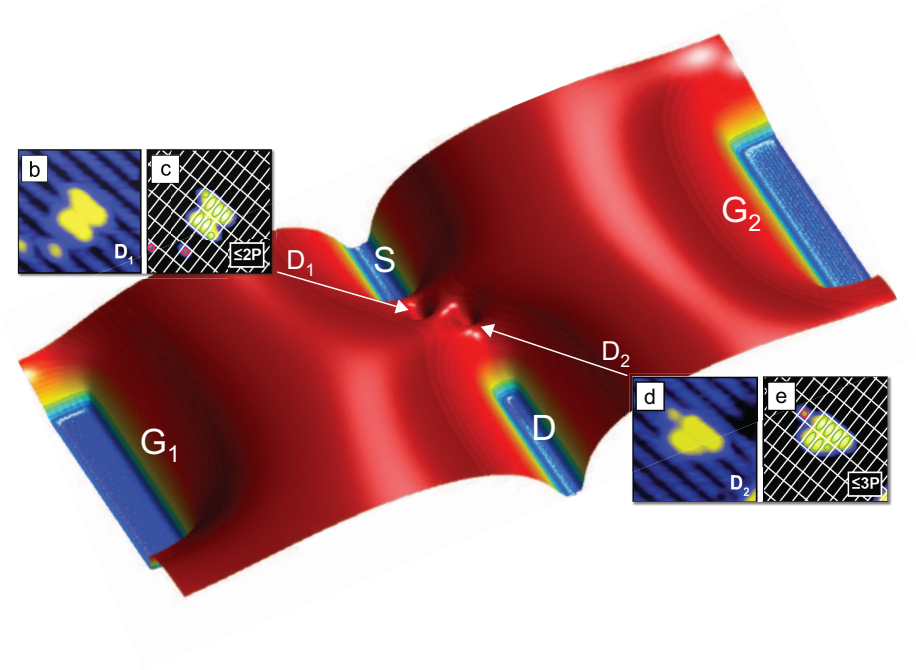

Fig. 3.2. Potential profile schematic of experimental double donor-dot device. b)-e), STM images of D1 and D2. Both dots extend across two adjacent dimer rows of the silicon surface with lengths of 2.5 - 4 contiguous dimers.

configuration finder module is based on combinatorial and custom-built algorithms and builds the foundation of the subsequent modeling modules.

In detail, the code first matches each possible donor location in the silicon crystal a unique identification or tile number. The geometric structure information of the dimer is translated into the code through boundary conditions between tiles. 3D spatial diffusion regions surrounding the core dimer region can also be dynamically added to match realistic device conditions. After the geometric structure has been translated into the model successfully a combinatory algorithm then determines all possible permutations of tile numbers depending on the number of donors in the system.

Physically unrealistic configurations (e.g. two donors one Si bond length apart) are filtered out via predefined tile occupation rules. After all valid donor configura-

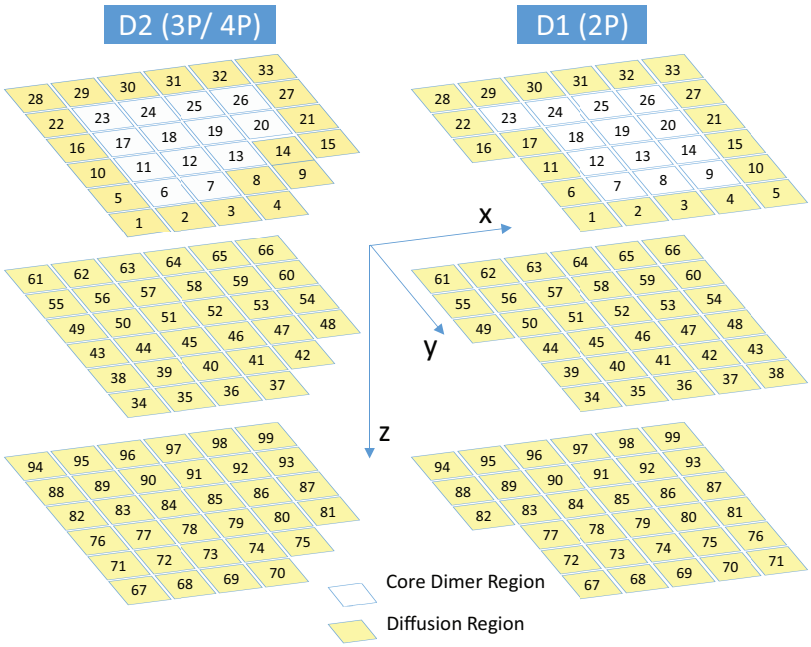

Fig. 3.3. Translation of quantum dots D2 and D1 into input deck tile structure. 3-D spatial diffusion beyond core dimer region increases quantum dot dimensions significantly. (not all tile planes shown) Each tile corresponds to a unique lattice point location in the silicon crystal structure. Core dimer and spatial diffusion tiles are shown in white and yellow, respectively.

tions have been identified, the configuration finder tool then proceeds to computing the inter-donor distance distribution function of the entire set of valid donor configurations. We define the inter-donor distance distribution function by summing the distances between donors for each configuration. Specifically, small inter-donor distance distribution function values correspond to close configurations with high binding energies, whereas large inter-donor distance distribution function values describe spread out donor configurations with lower binding energies. The inter-donor distance distribution function is of central importance throughout the entire modeling process. The function breaks down the complexity and information load of a donor configuration in 3D space into a single number, thus reducing computational memory requirements significantly. At the same time the inter-donor distance distribution

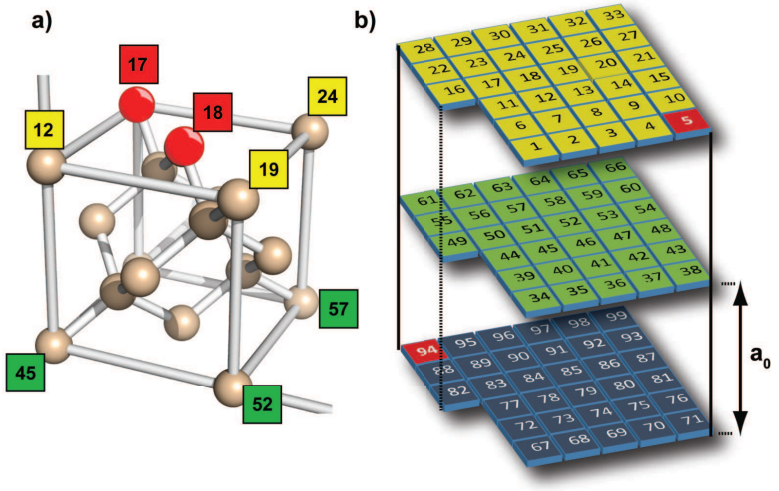

Fig. 3.4. Input deck tile structure of the experimental dimer quantum dot D1. (a) Silicon crystal lattice positions matched with tile numbers. Tile combination 17-18 (red) shows minimum allowed donor separation between 2 phosphorus donors. (b) 3-D input deck structure of experimental 2P dimer quantum dot with a total of 99 unique tile positions (not all planes shown here). Tile combination 5-94 shows maximum possible donor separation within the spatial quantum dot dimensions.

function is able to retain sufficient information of the underlying real space donor configurations to allow accurate large-scale empirical modeling.

Depending on the size of the dimer and number of donors, the number of possible configurations can be in the range of hundreds of millions. Handling of such a large data set can be challenging. To reduce the amount required data storage, the configuration finder module executes symmetry comparison algorithms to segment configurations into sets of unique translationally invariant configurations.

The symmetry comparison algorithm is one of the most time intensive parts of the modeling process. To improve performance of the algorithm several techniques have been employed or are currently under development. For example, the model first arranges the entire configuration space as a function of the inter-donor distance distribution function. As translationally invariant configurations must have the same

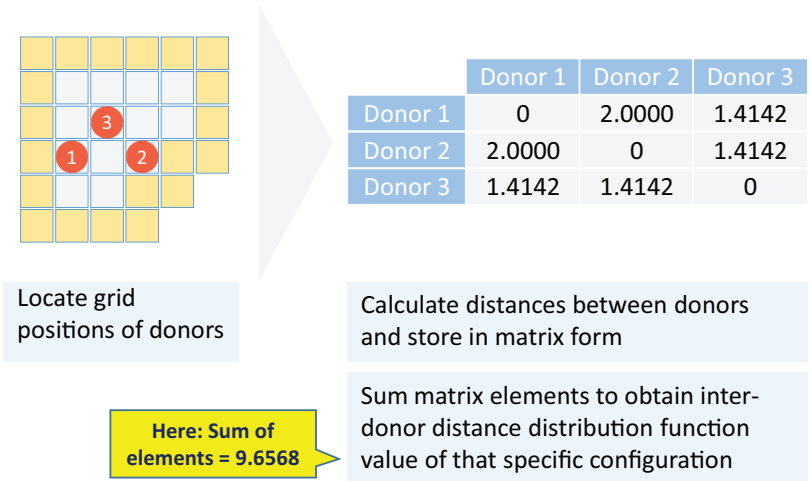

Fig. 3.5. Inter-donor distance distribution function. Definition and example of inter-donor distance distribution function for a sample donor configuration. (1) Locate exact grid positions of donors in silicon crystal lattice. (2) Compute inter-donor distances from each donor location and save in inter-donor distance matrix. (3) Sum all elements of inter-donor distance matrix to obtain inter-donor distance distribution function value for specific donor configuration.

distribution function value, this allows for dramatically reducing the required computational search scope for each array iteration. Furthermore, the code assigns each set of translationally invariant donor configurations a unique identifier or flag. Donor configurations, which have been flagged are excluded from the search scope in subsequent search iterations. Besides improving code execution performance significantly, the completed flagging process results to a powerful filter for mapping out the distribution of unique donor configurations across the entire configuration space.

3.3.3 1e Binding Energies

If the number of unique configurations is small enough (e.g. 10-100), we can use atomistic tight-binding simulations to calculate the unique 1e binding energies and then extrapolate these results into the entire configuration space. More often though, the number of unique configurations is beyond the practically feasible scope for ex-

Table 3.1
Number of possible and unique D1(2P) and D2(3P/4P) donor cluster configurations. The number of configurations grows quickly for increasing number of donors, rendering explicit atomistic calculation of binding energies practically infeasible.

Donor #	All Configurations	Unique Configurations
2P	30,983	89
3P	2,507,483	15,469
4P	149,664,630	3,562,341

plicit atomistic calculation. For larger dimers and donor numbers such as 3P/4P dimers and with consideration of 3D spatial donor diffusion effects, the number of unique configurations can still be in the range of millions and too large for an atomistic tight binding approach. We thus developed an empirical models for predicting 1e binding energies of millions of configurations based on an extensive dataset of atomistically calculated 1e binding energies. In particular, the inter-donor distance distribution function is strongly correlated to atomistically calculated 1e binding energies, which can be empirically quantified by inverse power law or multi-polynomial formulas. Using the configuration finder tool and empirical functions deduced from a limited set of atomistic tight-binding calculations, the code is thus able to calculate 1e binding energies for millions of configurations. Furthermore, analysis of the distribution function allows quick identification of worst case configurations. Small distribution function values correspond to close configurations with high binding energies, whereas large values describe spread out donor configurations with lower binding energies.

3.3.4 Higher Binding Energies

A key challenge towards modeling of multi-million configuration confidence bands is reducing the computational costs of calculating higher electron binding energies. We thus developed empirical models, which allow rapid iterative calculation of higher electron binding energies for large numbers of configurations. Detailed statistical analysis of our atomistically calculated dataset of higher electron number binding energies confirmed that the relative percentage drop of binding energies with increasing number of electrons is strongly correlated. Specifically, if $E_B(\mathrm{N})$ is the binding energy of the Nth electron for a donor cluster, the percentage change in binding energy between the N+1 and the Nth electron was found to vary linearly with $E_B(\mathrm{N})$ for all N. This enables us to extrapolate the higher electron binding energies for a large number of cluster configurations by using linear fitting functions.

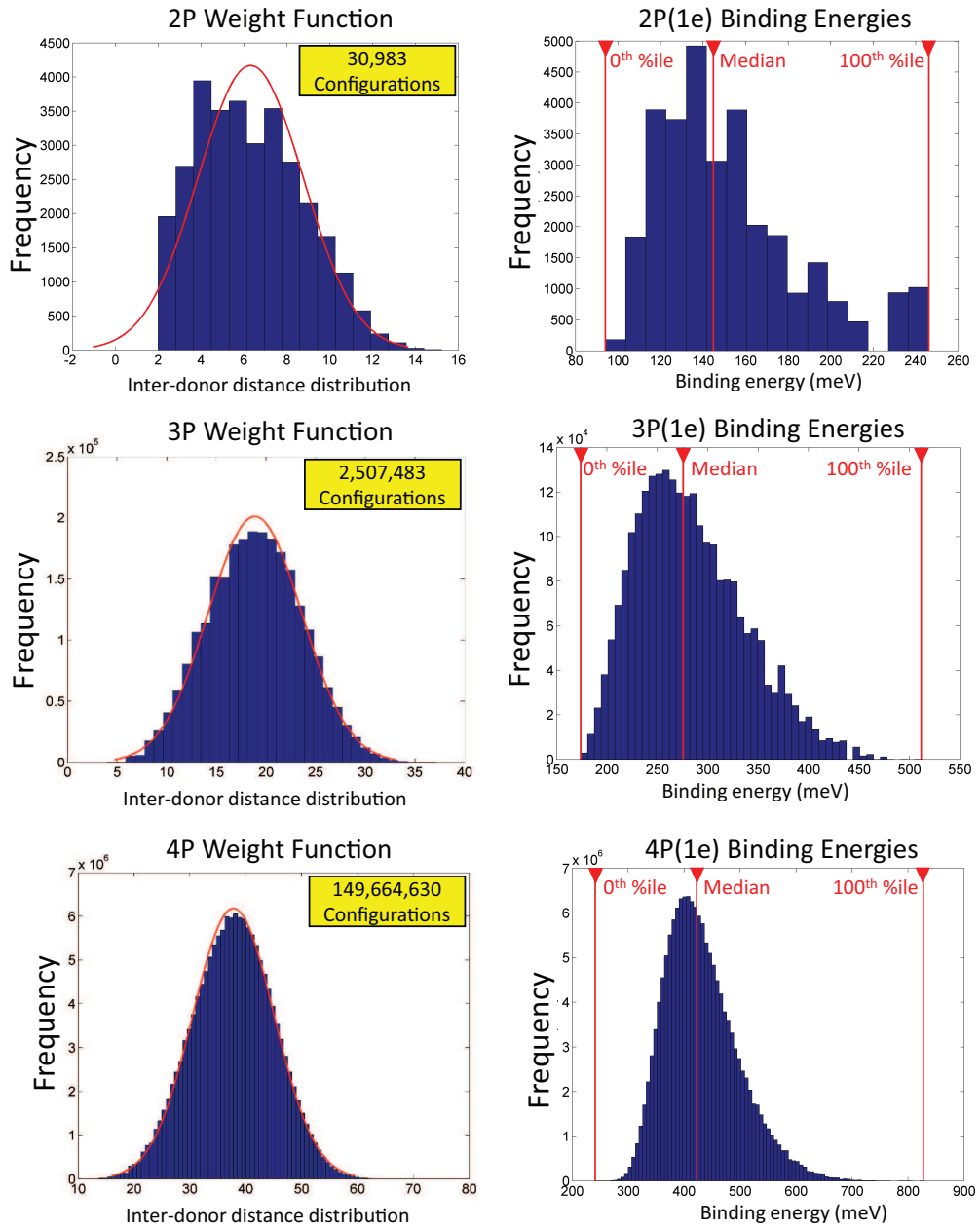

Fig. 3.6. Inter-donor distance distribution functions and corresponding 1e binding energy distributions for 2P, 3P and 4P dimers.

3.3.5 Binding Energy Confidence Bands

By combining the results from all the modules we can compute statistically weighted binding energy confidence bands encompassing millions of donor configurations. Here,

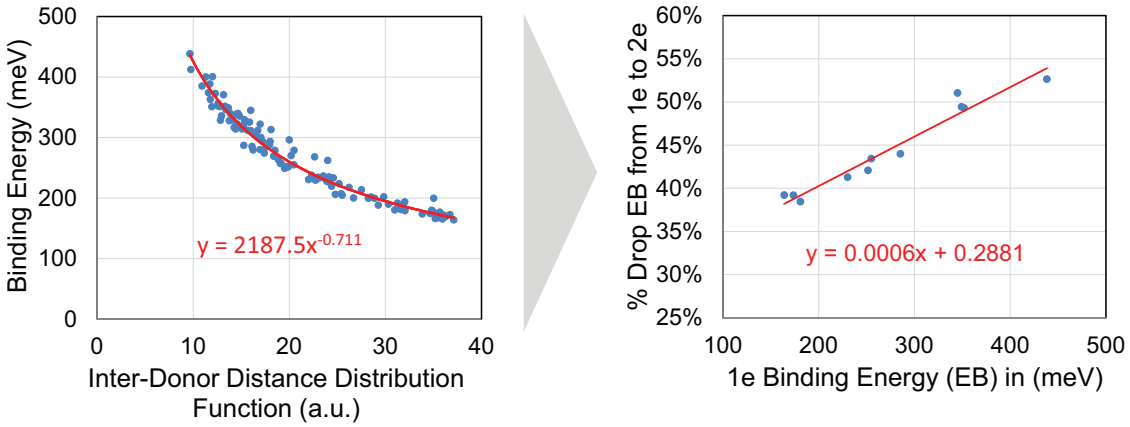

Fig. 3.7. Empirical formulas for 3P donor cluster enable rapid generation of binding energy confidence bands from a limited set of atomistic simulations.

an extensive and still growing database of atomistically calculated donor configurations for various dimers and donor numbers provides the backbone for accurate empirical models.

Figure 3.9 shows the final binding energy confidence bands as obtained from the confidence band generator module. The combined confidence bands of the experimental quantum dots D2 and D1 comprise together more than 150 million possible donor configurations. The shading of the bands indicates the relative probabilistic distribution of donor configurations within the confidence bands. We see that the spread of the confidence bands reduces quickly with increasing electron numbers. Furthermore, dimers with larger donor numbers (3P/4P) show greater spread and cross-overlap with other confidence bands. Worst case donor configurations corresponding to very close or widespread donor configurations spread the confidence bands significantly, but are found to typically account for less than 10% of possible donor configurations.

Analytical Binding Energy Formulas

$$EB_{p,x}\,[meV] = \alpha\,[meV] * (Average\ interdonor\ distance\ [nm])^{-\beta},\ x=1,\ p>1$$

$$EB_{p,x}\,[meV] = \left[1 - \left(\alpha\left[\frac{1}{meV}\right] * EB_{p,x-1}[meV] + \beta\right)\right] * EB_{p,x-1}[meV],\ x>1,\ p>1$$

Fitting Parameters

# donors p	# of electrons x = 1	x = 2	x = 3	x = 4
p=2	α =156.44 β =0.474	α =0.0011 β =0.3768	α =0.0056 β =0.2601	α =0.0172 β =0.5459
p=3	*α =309.04* *β =0.706*	*α =0.0006* *β =0.2892*	*α =0.0013* *β =0.2660*	*α =0.0030* *β =0.3168*
p=4	*α =480.98* *β =0.768*	*α =0.0003* *β =0.2576*	*α =0.0005* *β =0.2183*	*α =0.0004* *β =0.3119*

Fig. 3.8. Analytical binding energy formulas for calculation of binding energies for 2P, 3P and 4P donor clusters with varying number of electron numbers. The formulas have been empirically deduced from a dataset of atomistically calculated binding energies. The formulas are generally valid independent of the donor cluster geometry and spatial diffusion effects and can be used for first order approximations of donor numbers, binding energies and electron numbers in phosphorus donor-based clusters. The first formula estimates 1e binding energies using the average inter-donor distance of a cluster configuration. The second formula iteratively calculates higher electron number binding energies. The fitting parameters and in both formulas are based on our calculated dataset of atomistic binding energies. Currently, our list of fitting parameters comprises clusters with up to 4 donors and 4 electrons.

3.4 Experimental Impact

In this section, we summarize the experimental impact of the double donor-dot device project in conjunction with the contributions of the hybrid modeling methodology. The following parts until section 3.5 are adapted from [1], *"Spin Blockade and*

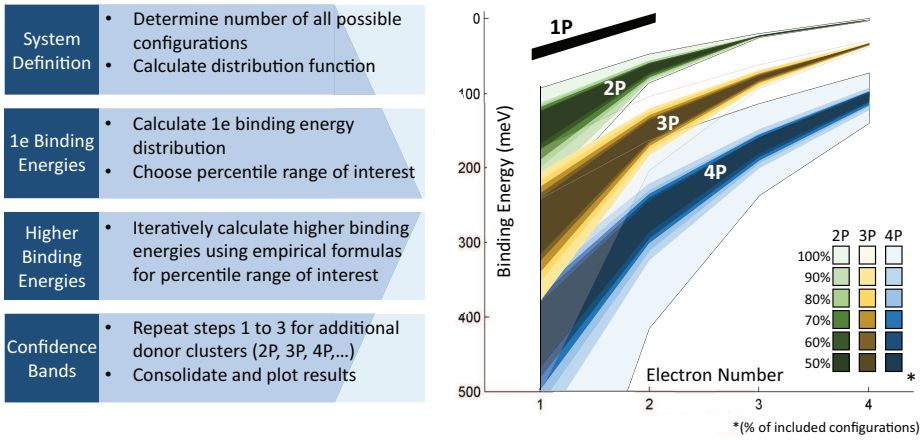

Fig. 3.9. Statistically weighted binding energy confidence bands computed using a hybrid atomistic/empirical modeling approach. The combined confidence bands show the statistical binding energy distribution of more than 150 million possible donor configurations. The spread of confidence bands reduces quickly with increasing electron numbers. Dimers with larger donor numbers (3P/4P) show significant confidence band overlaps, thus reinforcing need for statistically weighted binding energy distributions.

Exchange in Coulomb-Confined Silicon Double Quantum Dots", B. Weber, Y. H. M. Tan, et.al., Nature Nanotechnology, DOI:10.1038 (2014)

A major goal of donor-based quantum computing architectures is the development of donor spin-qubit arrays with individual qubit control using magnetic and electric fields. Here an understanding of the complex interplay between the electron's spin and charge degrees of freedom, such as spin to charge conversion or exchange coupling between qubits, is essential.

Whereas spin-to-charge conversion via Pauli spin-blockade has been achieved in few electron double quantum dots in silicon and GaAs architectures [34–36] [44] [45] it is yet to be observed in tunnel-coupled pairs of donors, [46, 47] the fundamental building-block of a scalable donor-based quantum computing architecture. Recent experiments in donor defined double quantum dots have demonstrated electron transport [46] and coherent manipulation of the charge degree of freedom [47] but to

date no signature of the spin degree of freedom has been reported. Here we demonstrate the depletion of a Coulomb-confined few-donor double quantum dot down to the last electron allowing the first demonstration of Pauli spin blockade in donor-based systems allowing us to measure the effective exchange interaction, providing an important step towards donor-based quantum computing architectures. The double donor-dot device was carefully characterised using atomic-precision STM fabrication techniques. The two dots are comprised of two (2P) and three (3) phosphorus donor atoms, placed within an all-epitaxial silicon device architecture.

3.4.1 A 2P/3P Quantum Dot System

The experimental silicon phosphorus device consists of a planar STM-patterned double quantum dot architecture. Charge confinement in the device is provided solely by the presence of the ionised donors, causing a lowering of local conduction band edge E_{CB}. Based on the STM images the upper bound for the number of donors incorporated into each dot template is estimated. Consistent with the 0.25 ML doping density previously observed, one can assume that a single P atom incorporates into every two consecutive dimers, and hence determine that ≤ 2 donors are incorporated in D1 and ≤ 3 donors in D2. The binding energies extracted from two different directional cuts through the 2D stability diagram (V_{G1}=1.3V_{G2} and V_{G1}=V_{G2}) are then compared theoretically modeled binding energy confidence bands for varying electron numbers on the dots and with different number of donors. The binding energies are calculated by considering all possible donor configurations in each dot for every donor number, taking into account lateral diffusion and vertical segregation of up to 1nm. The resulting range of binding energies obntained for different donor configurations is given by the shaded bands, representing the percentile likelihood of binding energies, based on inter-donor distance distribution functions. As can be seen the modeling binding energy confidence bands confirm that we have a 2P donor dot in D1 and a 3P donor dot in D2 in agreement with the high-resolution STM-images.

The Si:P donor-based quantum dots were modelled by constructing clusters of 2P, 3P and 4P donor atoms distributed at substitutional lattice sites within the lithographically defined quantum dot (Fig. 3.10cf) and were embedded within a 30 x 30 x 30 nm3 simulation domain of atomistic representation. Donor diffusion was also included into the modelling by taking into account diffusion of donors by $\sim$ 1 nm in all directions. Each individual donor was represented by a screened and truncated Coulomb potential at a substitutional lattice site, which was parameterized to give the experimental ground-state energy of 45.6 meV for Si:P [14]. The method applied to the calculation of the two-electron D- energy provided $\sim$ 2 meV binding energy, in close agreement with the experiments. The n-electron groundstate energies for different donor dots were subsequently obtained through self-consistent charge-potential SchroedingerPoisson calculations, with electronelectron interaction effects taken into account through a local density approximation (LDA) ansatz. Binding energies are expressed with respect to the silicon bulk conduction band edge E_{CB}.

3.4.2 Observation of Spin Blockade

Figure 3.12 shows two sets of bias triangles, highlighted by white and red circles [1]. Close-ups of these transitions are shown in Fig. 3.13a,b, recorded at V_D=$\pm$5 mV and $\pm$3mV, respectively. As seen in the data, the first set of triangles at the (1,2) $\rightarrow$ (0,3) transition (white circle, Fig. 3.13a) is symmetric upon bias reversal, showing a well-pronounced ground state resonance at the triangle base, as expected as a single, unpaired valence spin tunnels freely through both dots at either S/D bias polarity. In contrast, at the (1,3) $\rightarrow$ (0,4) transition (red circle, Fig. 3.13b) we find rectifying behavior with a strong suppression of current at negative bias polarity. This provides a clear signature of spin blockade where at this transition only a single electron spin resides on D1 with an unpaired valence spin on D2 (Fig. 3.13b). Electron transport at this transition can therefore only proceed in the sequence (0,3) $\rightarrow$ (1,3) $\rightarrow$ (0,4) $\rightarrow$ (0,3) if both spins are antiparallel (that is, are in a singlet state). Current is

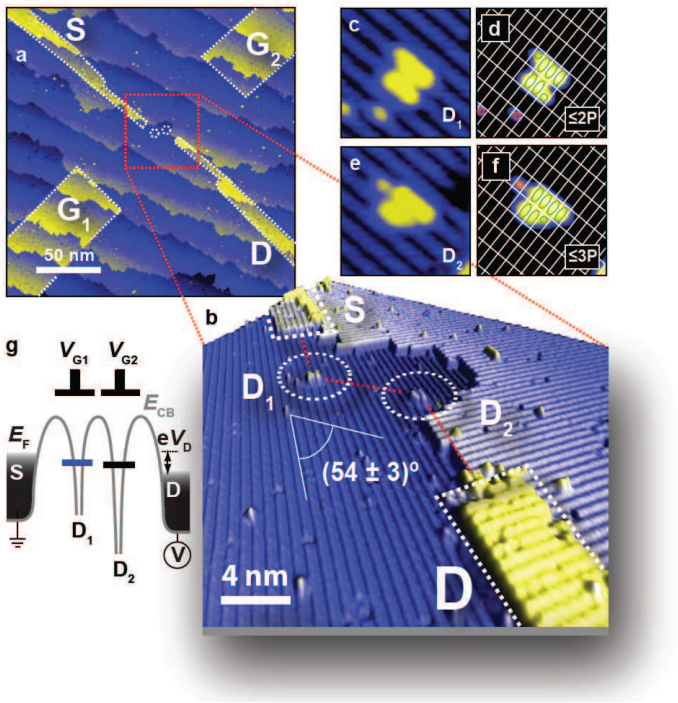

Fig. 3.10. Experimental double quantum dot device [1]. a) STM images of a donor based double quantum dot device template after STM lithography, showing source (S), drain (D) and gate (G1,2) electrodes. b) The central part of the device hosts two atomic-scale quantum dots (D1, 2), symmetrically placed at a distance of 11.5 nm between the S/D leads. c)-f), Atomic resolution STM images of D1 and D2. Both quantum dots extend across two adjacent dimer rows of the silicon surface with lengths of 2.5 - 4 contiguous dimers (green ellipses). g) Schematic of the potential profile of the device defined by local variations of the silicon conduction band edge along a cut following the dashed red line in b. Charge confinement is given by a combination of individual donor Coulomb potentials tightly distributed within the dots.

blocked if the spins are aligned (that is, in a triplet state), with spin-selection rules prohibiting the occupancy of the (0,4) charge state. As a result, the double quantum dot becomes stuck in a metastable spin triplet state, not allowing current from S to D. Clear lines of finite $\sim$ 300 pA current at the edges of the bias triangles in Fig. 3.13b arise when the (1,3) spin states are within the thermal window of the source electrochemical potential, allowing spins to be exchanged with the S/D leads, lifting

the blockade [36]. This behavior demonstrates Pauli spin blockade and even-odd filling as previously observed in few-electron GaAs/AlGaAs [36] and silicon double quantum dots with lifted valley degeneracy [44, 45].

3.5 Conclusions

We have observed Pauli spin blockade and exchange coupling in transport through a few-electron, donor double quantum dot. The two dots are composed of two (2P) and three (3P) donor atoms, placed with atomic-precision control within an all-epitaxial silicon device architecture. The precise donor and electron numbers were confirmed by finite bias spectroscopy, STM imaging and atomistic TB calculations. We have demonstrated that we can apply large enough electric fields to overcome the inherently large charging energies in donor dots to transfer both electron spins onto the same dot. Consequently, we observe spin blockade at the (1,3) $\rightarrow$ (0,4) charge transition, involving a single electron spin on the 2P dot that forms effective two-spin singlet and triplet states with an unpaired valence spin (n=3) on the 3P dot. These results allow us to estimate the effective exchange interaction at the hybridization point between Coulomb-confined electron spins, providing an important step on the road to two-spin logic gates in donor-based quantum-computing architectures.

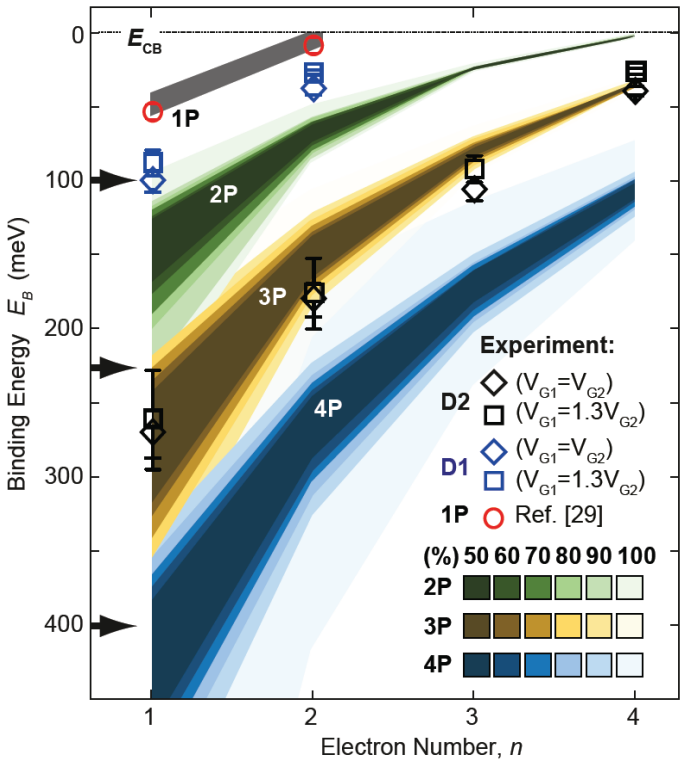

Fig. 3.11. Comparison of measured binding energy spectra of few-donor double quantum dots with self-consistent atomistic/empirical tight-binding calculations [1]. The measured spectra of D1 (blue diamond, $V_{G1} = V_{G2}$); blue square, $V_{G1} = 1.3V_{G2}$) and D2 (black diamond $V_{G1} = V_{G2}$; black square, $V_{G1} = 1.3\ V_{G2}$), as well as a previously published single atom transistor [9] show good agreement with atomistic calculations of binding energy spectra. This allows identification of D1 and D2 as 2 and 3 P-donor dots (shaded bands), showing clear differences to the known binding energy of a single P donor. The widths of the shaded bands in the modelling reflect the respective variations in binding energies due to different spatial distributions of donors within each dot, taking a diffusion length of 1 nm into account. Variations from these two directional cuts are less than the experimental error bars (±3 meV to ±34 meV), arising due to the uncertainty in the absolute position of ECB and the lever arm, α. The lever arm for each cut was extracted from the diamond edges [28] at each charge transition and found to decrease slightly with increasing gate-voltage from $\alpha = 0.22$ for the first electron on D2 to $\alpha = 0.18$ for the second (fourth) electron on D1(D2). For each measured binding energy $E_{B,D1(2)}(n)$ we have therefore taken an average over the range of gate voltages up to the respective transition.

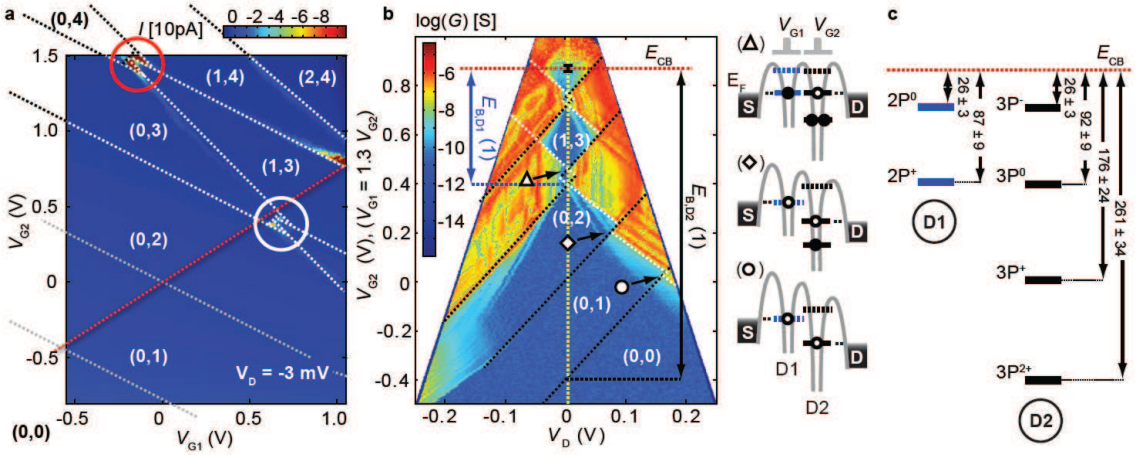

Fig. 3.12. Spectroscopy of a donor-based few-electron double quantum dot [1]. a) The charge stability diagram (VD = 3 mV) showing the drain current of the device as a function of both plunger gates G1(2), demonstrating independent electrostatic control over the individual dots. b) The total electron numbers (n,m) as well as n-electron binding energies, $E_{B,D1(2)}(n)$, have been determined in finite bias spectroscopy measurements from a diagonal cut through (a) along the dashed red line. The accompanying schematics show the alignment of the respective dot electrochemical potentials as well as electron occupations at the three positions highlighted by ▲, ♦, and ●. The dashed white (black) lines bounding the Coulomb diamonds indicate the alignment of the D1(2) electrochemical potentials with the S(D) Fermi levels, respectively. The horizontal red dashed line in b indicates the approximate position of the silicon conduction band edge. c) Measured binding energy spectrum of D1 and D2.

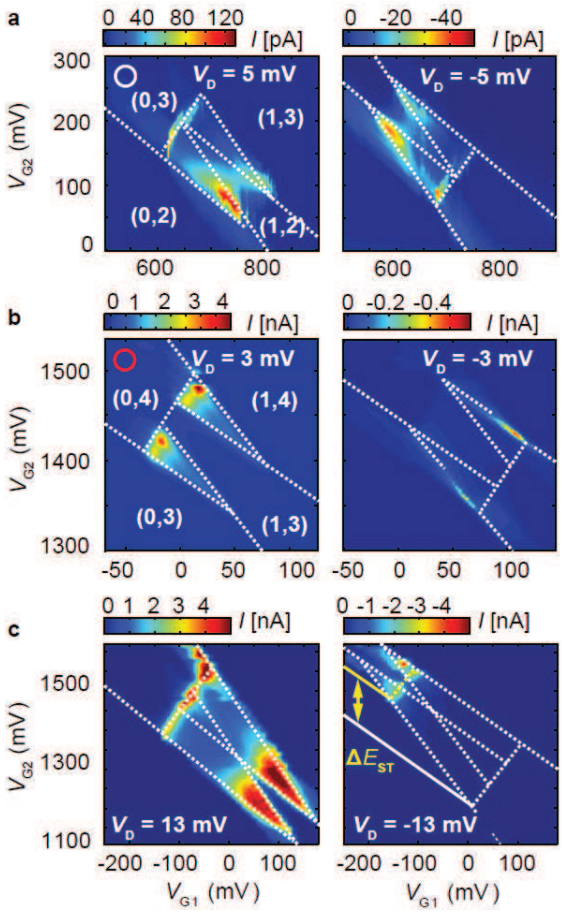

Fig. 3.13. Observation of spin blockade [1]. a-b), Close-ups of the (1,2) (0,3) and (1,3) (0,4) transitions as highlighted by white and red circles respectively in Fig. 3.12. Spin-blockade is observed at the transition with an even electron number (b), involving a single spin, on the D1 and an unpaired spin in D2. No blockade is observed at the odd electron numbers, supporting the conventional picture of spin blockade due to effective two-spin singlet and triplet states. Clear lines of current along the outer edges of the triangles result from spin-exchange with the S/D electrodes. c) Measurement of the singlet-triplet splitting Δ_{ST} (8±1) meV

4. LARGE-SCALE ATOMISTIC MODELING OF SILICON PHOSPHORUS NANOWIRES

4.1 Abstract

This work highlights the results of large-scale atomistic modeling of highly doped silicon phosphorus (Si:P) nanowires. Si:P nanowires of up to 10nm length are modeled, for the first time, with consideration of long-range atomistic dopant placement disorder effects. Our theoretical results corroborate experimentally observed breakdowns of metallic conduction in highly doped Si:P nanowires due to dopant placement disorder induced charge carrier localization.

4.2 Introduction

Highly doped silicon phosphorus nanowires have emerged as promising candidates for future ultra-scaled interconnects. Recent advances in the fabrication of atomic-scale devices using STM lithography, have demonstrated that highly doped silicon phosphorus nanowires can exhibit metallic like conduction [15]. In specific, Weber et.al. [15] found these highly doped Si:P wires to maintain a diameter-indepepdent bulklike resistivity as low as rho3D=(0.3 plus minus 0.2) mOhmm at T=4.2K.

Atomistic self-consistent tight-binding calculations have confirmed metallic conduction in highly doped Si:P nanowires [25]. However, these simulations described the wire as a system of periodic repetitions of short doped supercells. Although the supercells addressed dopant disorder, the limited length of the supercells was not sufficient to resolve long-range dopant disorder effects.

Realistic modeling and understanding of dopant disorder is crucial since it can lead to spatial charge carrier localization [53] and eventually imposes a limit to metallic conduction observed in low-dimensional nanostructures [52].

In this chapter, we present a detailed study of long-range dopant disorder effects in highly doped silicon phosphorus (Si:P) nanowires. Using extensive atomistic modeling and experimental data [52], we are able to simulate Si:P nanowires of up to 10nm length with 26 donor impurities with atomic-scale resolution.

Our theoretical results corroborate experimentally observed breakdowns of metallic conduction in highly doped Si:P nanowires due to dopant placement disorder induced charge carrier localization [52].

The first section of this chapter introduces the experimental Si:P nanowire and observed dopant disorder induced conduction fluctuations.

The subsequent sections focus on the modeling methodology and modeling results.

4.3 Experimental Si:P nanowire

This experimental section has been adapted from [52]. *Limits to Metallic Conduction in Atomic-Scale Quasi-One-Dimensional Silicon Wires, B. Weber, H. Ryu, Y.H.M. Tan, et. al., PRL 113, 246802 (2014)*

In figure 4.1, STM images of the two Si:P wires (W_1) and (W_2) are shown, with high-resolution closeups in Figures 1(c) and 1(d). The lithographic widths of the wires W_1 and W_2 are w = 4.6 nm and w = 1.5 nm, respectively. The wires are almost identical in length (L(W_1) = 47 nm and L(W_2) = 49 nm between the contacts). The subsequent modeling work will focus on the thinner wire W_2.

Figures 4.1(e,f) show four-terminal IV measurements of the two wires at T = 4.2K. In the thicker wire (W1), wee see linear IV curves and a weak dependence on gate voltage. This indicates metallic conduction with large carrier density screening the gate-induced electric fields.

Four-terminal IV characteristics at T = 4.2 K are shown in Figs. 4.1(e) and 1(f). In the 4.6 nm wide wire (W1), linear IVs and a weak dependence on gate voltage indicate metallic conduction with the large carrier density effectively screening the gate-induced electric fields. In comparison, the 1.5 nm wide wire (W2) shows a strong dependence on gate voltage and tunability of the device from Ohmic to non-Ohmic. The wire thus W2 indicates incomplete screening of the disorder potential and carrier localization.

In figure 4.2, we plot the conductance G_W corrected for series resistances arising within the contact triangles at either end of the wires. The lower panel in each figure shows conductance at $V_{4T} = 0$ V, with respect to $G_0 \sim e^2/h$ (black dashed lines).

In the 4.6 nm wide wire (W1) the absence of conductance features resembles the characteristics of an Ohmic resistor with $G_W > e^2/h$ at all gate voltages. Metallic conduction is confirmed by the approximately linear slope.

In the 1.5 nm wide wire (W2) in figure 4.2(b), we observe regions of reduced differential conductance around zero bias and at negative gate voltage. These result in regular oscillations in the linear conductance G_W, and arise from Coulomb blockade of strongly localized carriers.

4.4 Modeling Methodology

In this section, we introduce the theoretical methodology for the atomistic modeling of highly doped silicon phosphorus nanowires.

The theoretical study's aim is to corroborate indications of charge carrier localization observed in the experimental nanowire W2. The following modeling work will focus exclusively on wire W2.

Since we want to investigate the influence of dopant disorder on charge carrier localization, an explicit atomistic representation of the dopants in the wire is necessary [25].

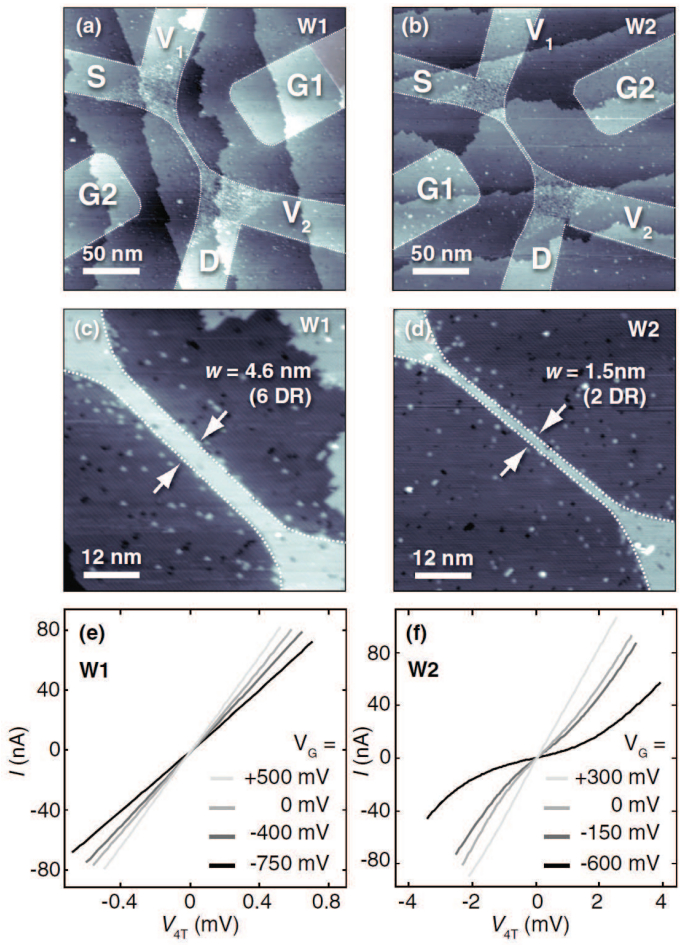

Fig. 4.1. Experimental Si:P nanowires [52]. (a) and (b) Overview STM images of two atomic-scale wires (W1) and (W2) with two contacts (S, V_1) and (D, V_2) on either end, allowing four-terminal (4T) resistance measurements. In-plane gates, G_1 and G_2, allow us to tune the electron density. (c),(d) Atomic resolution images show the alignment. The lithographic widths, w = 4.6 nm (W1) and w = 1.5 nm (W2). (e),(f) 4T IV characteristics at T = 4.2 K and for varying gate bias, V_G.

We use atomistic self-consistent tight-binding calculations to model the bandstructure, density of states and charge profiles of silicon phosphorus doped nanowires [25].

Figure 4.3(a) shows the simulation domain in NEMO for W2. The nanowire (red) is surrounded by a buffer region with dimensions x,y and z. The size of the buffer

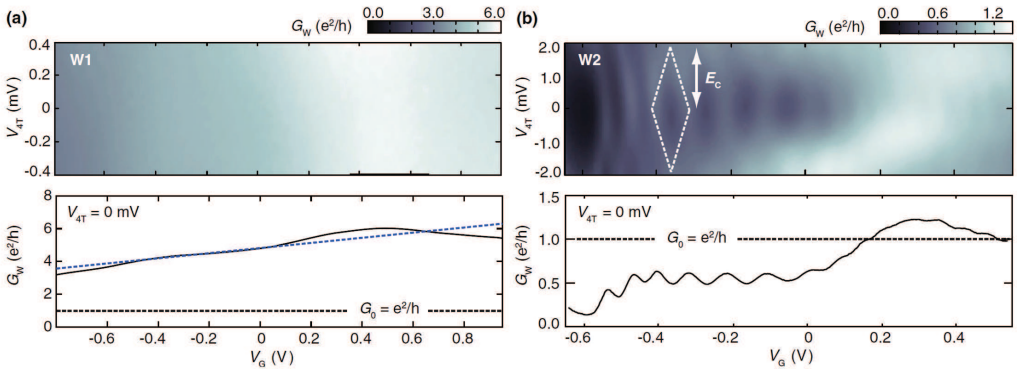

Fig. 4.2. 4T differential conductance GW of two atomic-scale wires W1 (a) and W2 (b) [52]. Upper panel: G_W as a function of gate voltage V_G, and 4T voltage drop,V_{4T}. Lower panel: Conductance, $G_W(4T = 0V)$ with respect to G_0 e^2/h (black dashed lines). The dashed blue line in (a) shows a linear fit to extract electron mobility. Coulomb blockade oscillations (b) are observed in the 1.5 nm wide wire (W2).

region has to be chosen sufficiently large to prevent boundary effects from altering physics in the central wire region.

Figure 4.3(b) shows an atomistic representation of wire W2 in NEMO with a sample uniform doping profile. As in the experiment, W2 in NEMO has dimensions of width w=1.5nm, a variable length y and a thickness of 1 atomic monolayer (ML).

To study the effect of long-range dopant disorder, we simulate a series of wires with different doping profiles and varying lengths y.

An overview of the different simulated wire configurations is summarized in figure 4.4. We analyze a total of 5 wires with lengths in transport direction and number of donors of up to 10 nm and 26, respectively. All nanowires have width w = 1.5nm corresponding to the experimental wire length of W2. In the atomistic calculation, periodic boundary conditions are assumed in the y transport direction. We investigate both ordered/uniform and disordered doping profiles. Furthermore, different buffer size dimensions are analyzed to identify and prevent boundary effects from impacting the central wire region simulation domain.

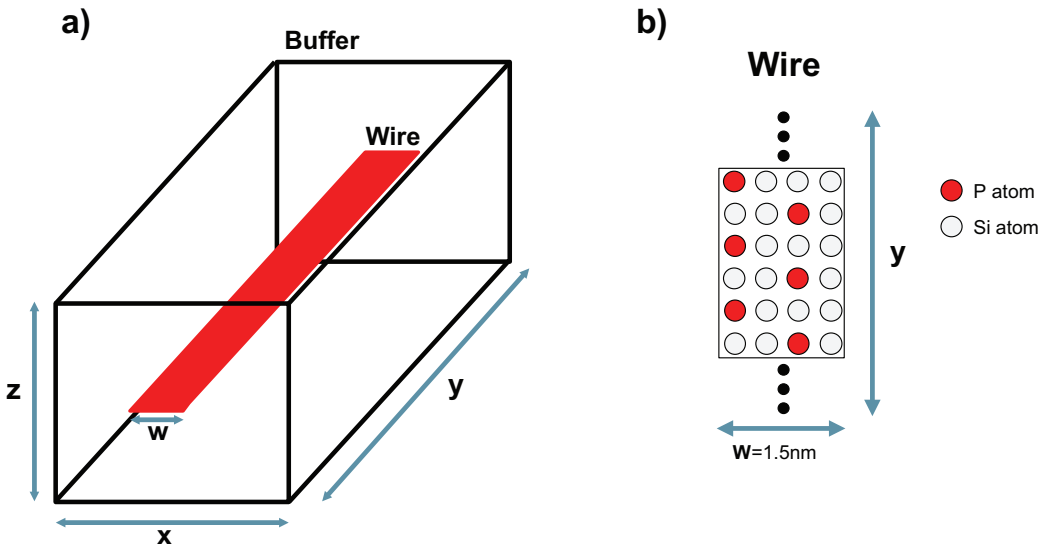

Fig. 4.3. a) General modeling domain for nanowire simulations in NEMO. The nanowire (red) is surrounded by a buffer region with dimensions x,y and z. b) Atomistic representation of nanowire in NEMO with sample uniform doping profile. The wire has dimensions of width w=1.5nm, a variable length y and a thickness of 1 atomic monolayer (ML).

4.5 Modeling Results

Previous tight-binding calculations of highly doped silicon phosphorus nanowires were limited to supercells with ∼2 nm length in transport direction [25]. In these calculations, the supercells were not long enough to resolve charge carrier localization due to long-range dopant disorder effects.

In this section, we present simulation results of an extensive atomistic study of highly doped silicon phosphorus nanowires. We are able, for the first time, to identify indications of long-range dopant disorder effects in these Si:P nanowires using atomistic modeling.

Furthermore, our theoretical findings support experimental observations of charge carrier localization and limits of metallic conduction in highly doped Si:P nanowires due to long-range dopant disorder effects [52].

	Wire length	Buffer		Doping	
Wire ID	**Length (y, nm)**	**Width (x, nm)**	**Height (z, nm)**	**Doping profile**	**# of dopants**
A	5.4	8.9	7.7	Ordered	14
B	10.0	8.9	7.7	Ordered	26
C	10.0	16.6	16.3	Ordered	26
D	5.4	16.6	16.3	Disordered	14
E	10.0	16.6	16.3	Disordered	26

Fig. 4.4. Overview of simulated nanowires. We model atomistically a total of 5 wires with lengths and number of donors of up to 10 nm and 26, respectively. Both ordered/uniform and disordered doping profiles are investigated. Width x and height z describe the buffer region, which encloses the nanowire. All nanowires have width w = 1.5nm.

Considering the substantial computational resource requirements of atomistic calculations, the buffer region around the central wire region has to be minimized as much as possible to enable simulation of longer supercells.

In figure 4.5 we benchmark the bandstructure and density of states (DOS) results of uniformly doped Si:P wires with varying buffer size dimensions and lengths. The goal here is to find optimal minimum buffer dimensions for the 10 nm long nanowire, which do not cause buffer boundary effects on the central wire region.

Figure 4.5 (a) shows wire A, a 5 nm long wire with uniform doping and buffer dimensions of x = 8.9 nm and z = 7.7 nm. Wires B and C in figure 4.5 (b) represent 10 nm long wires, also with uniform doping profiles. Wire B exhibits identical buffer dimensions as wire A, whereas wire C has larger buffer dimensions of x = 16.3 nm and z = 16.6 nm. The bandstructure and DOS results of wire A (figure 4.5 c) are free of boundary effects from the buffer. We can thus conclude that for the shorter wire A, the buffer is sufficiently large.

In contrast, if we increase the length of the wire to 10 nm while maintaining the same buffer dimensions as we go from wire A to wire B, wee observe artifacts in the DOS (figure 4.5 d). Here, the now extended central wire region interacts with the buffer boundaries, which leads to lifting of degeneracies in the lower bands of the bandstructure at k=1.

To ensure results accuracy, it is necessary to scale up buffer dimensions for longer wires. For wire C, we thus increase the buffer dimensions while keeping the wire length constant at 10 nm. In figure 4.5 (e) depicts the bandstructure and DOS calculations of wire C, which are now absent of buffer boundary induced artifacts.

In the following, we shift focus to disordered dopant profiles. Figure 4.6 shows the disordered doping profiles of wires D and E. Wire D is 5.4nm long and has 14 dopants. Wire E is 10nm long and has 26 dopants. The buffer dimensions of wires D and E correspond to wires A and C, respectively.

Plots of the atomistically calculated bandstructure and density of states (DOS) of wires D and E are shown in figures 4.6 (c, d). For the 10 nm long disordered wire E, we observe a gap in the DOS. Even though the DOS gap is below the Fermi level, the emergence of this DOS gap corroborates experimental findings of onsets of charge carrier localization in longer nanowires. Importantly, we did not observe DOS gaps for the 10nm long and uniformly doped wire C (see figure 4.5), which indicates that dopant disorder is responsible for the DOS gap.

Comparing the DOS profiles of both disordered wires D and E, which differ only in length y, we also see that wire supercells have to be sufficiently long to resolve long-range dopant disorder effects in the DOS.

Figure 4.7 shows the charge profiles of both wires D and E. Although both wire D and E have disordered doping profiles, only in the longer wire E do we observe noticeable charge carrier localization. In summary, our results conclude, in line with experiments, that charge carrier localization and the resulting limits in metallic conduction in highly doped Si:P nanowires is a function of doping randomness and wire length.

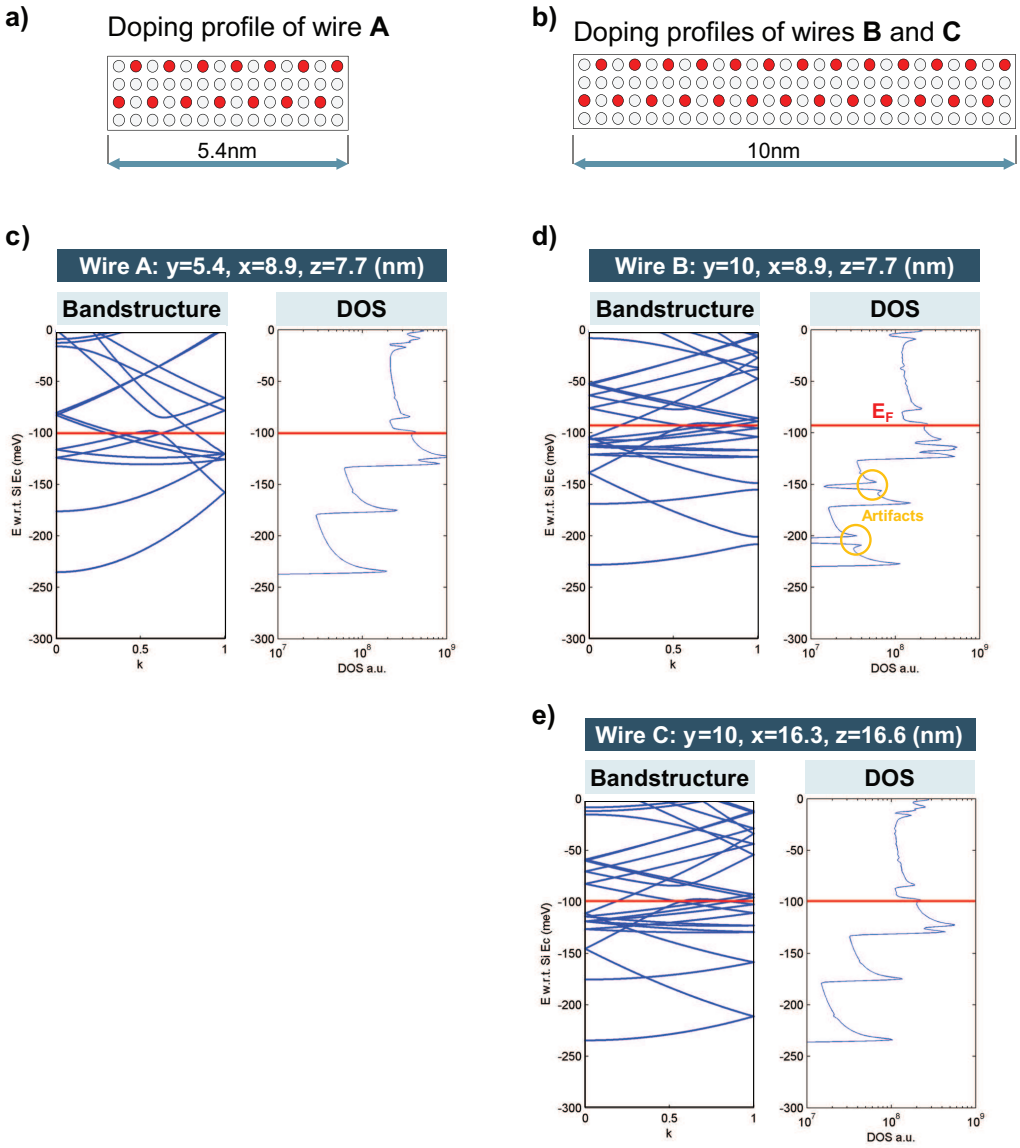

Fig. 4.5. a,b) Schematics of uniform doping profiles of wires A, B and C. Wire A has a length of y=5.4nm, wires B and C have lengths y=10nm. c,d,e) Bandstructure and density of states (DOS) plots for wires A, B and C. d) Results for wire B show artifacts due to insufficiently large buffer region. e) Artifacts disappear with choosing larger buffer dimensions.

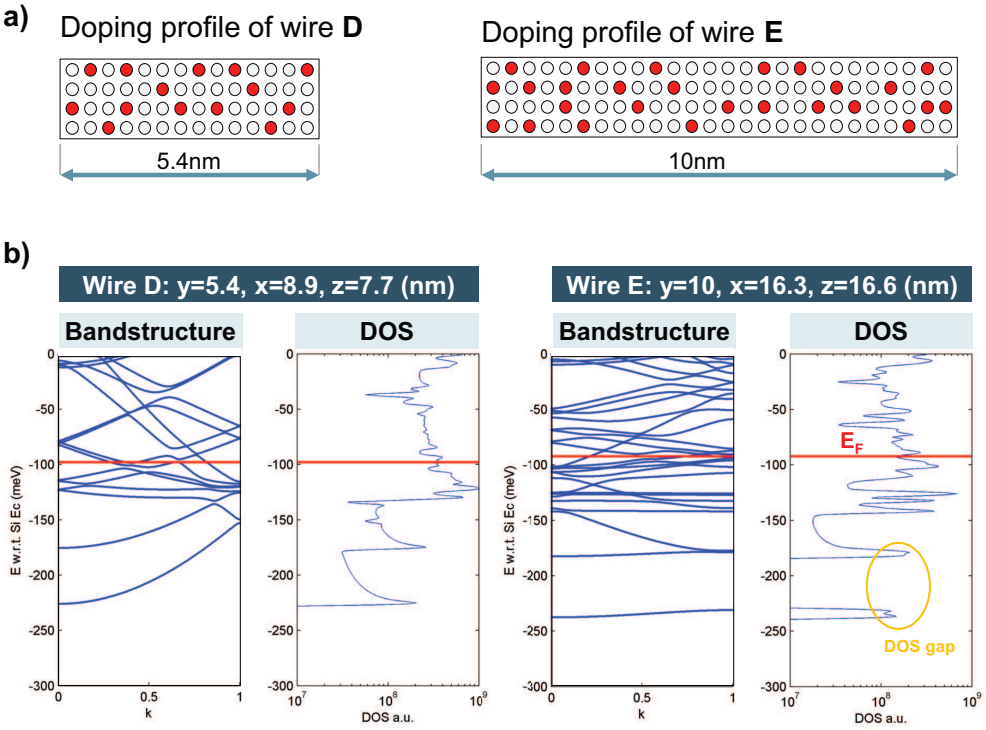

Fig. 4.6. a, b) Disordered doping profiles of wires D and E. Wire D is 5.4nm long and has 14 dopants. Wire E is 10nm long and has 26 dopants.c,d) Bandstructure and density of states (DOS) plots of wires D and E. d) At wire lengths of y=10nm, we see the appearance of a gap in the DOS. Even though the DOS gap is below the Fermi level, the observance of this DOS gap corroborates experimental findings of onsets of charge carrier localization in longer nanowires.

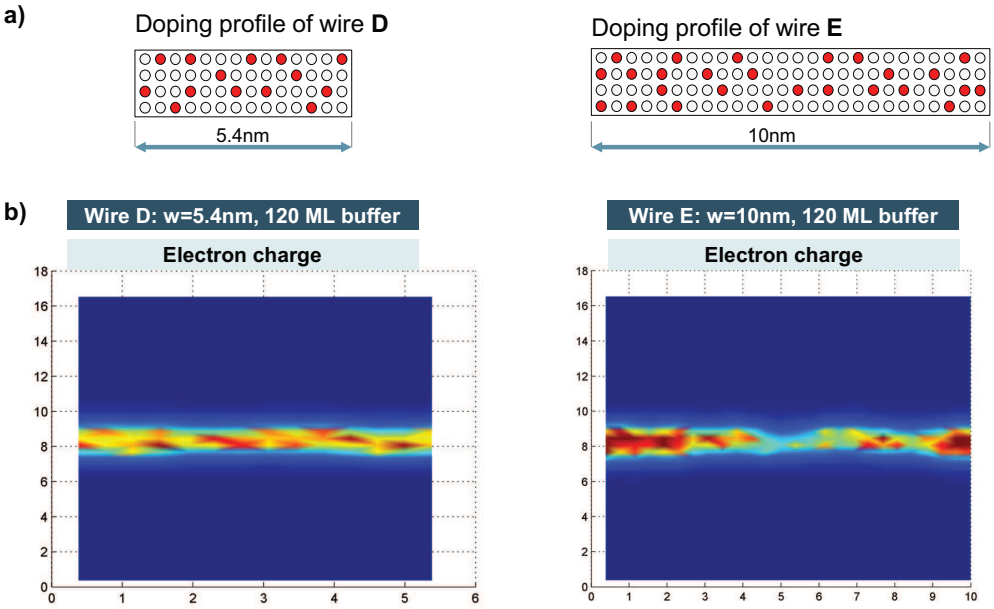

Fig. 4.7. a, b) Disordered doping profiles of wires D and E. c,d) Atomistically calculated charge density plots for wires D and E. c) No strong indications of charge carrier localization in the shorter disordered wire D. d) The disordered wire E shows indications of charge carrier localization. Results show that observation of charge carrier localization is a function of doping randomness and wire length.

5. FUTURE WORK

5.1 Abstract

This chapter presents proposed future work projects which build upon and expand the scope of empirical modeling for donor-based quantum computing architectures. The overarching goal is the development of a comprehensive and expandable set of hybrid empirical/atomistic models which allow high speed statistical device characterization of donor-cluster based quantum computing architectures. For achieving this goal, a three stages project plan is proposed.

Stage One: Diffusion Effects and 3-D Spatial Analysis of Donor-Clusters

Here, the motivation is to develop a deeper understanding of donor diffusion effects and the statistical distribution of worst case binding energy configurations as a function of donor cluster geometry. This work will provide design guidelines for optimal donor cluster geometries, and enable quantitative analysis of the impact of donor diffusion and fast statistical prediction of donor numbers.

Stage Two: Empirical Model Development for Hyperfine Coupling and Spin Decoherence

Hyperfine coupling and spin decoherence are important key metrics in quantum computing architectures and highly sensitive to atomic-scale doping fluctuations. The goal here is to develop empirical/atomistic models which will allow large-scale modeling of hyperfine coupling and spin decoherence times in multi-million configuration donor clusters.

Stage Three: A Modular Empirical/Atomistic High-Speed Modeling Tool

In the third stage, we plan to consolidate all empirical/atomistic models into one comprehensive model. By cross referencing the models, we vision rapid characterization of donor-clusters with unprecedented speed and comprehensiveness. This unified

empirical/atomistic model will enable highly accurate determination of donor numbers and atomic-scale triangulation of statistical binding energy, hyperfine coupling and spin decoherence confidence bands.

5.2 Diffusion Effects and 3-D Spatial Analysis of Donor-Clusters

5.2.1 Motivation

Despite the development of high precision fabrication techniques, inherent atomic-scale statistical variations of dopant placement can influence device behavior in donor-based devices considerably. Understanding statistical dopant placement variations is thus necessary for accurate device characterization on an atomic scale. Sub-nanometer diffusion of donors increases the effective dimensions of donor-clusters. In atomic-scale donor-based quantum computing devices, these donor diffusion effects can change predicted device behavior considerably. Addressing the innovation imperative for atomic-scale methods capable of modeling realistic dopant placement variations and donor diffusion effects using millions of donor configurations will close a major gap in current device characterization capabilities and provide important design guideline implications for future quantum computing devices.

5.2.2 Background

The double-donor device work resulted in the development of a novel hybrid atomistic/empirical modeling methodology [1]. The hybrid model currently consists of four modules, which combined together enable rapid computation of statistically weighted binding energy confidence bands. A modular coding approach was chosen intentionally to allow easy integration of future modeling features. For example, the configuration finder tool, which determines the number of possible donor configurations can accept any donor-cluster geometry, different weight functions and empirical models as input parameters. The confidence band generator can be fed with any distribution

proxy function (e.g. inter-donor distance weight function for binding energies) and empirical models. Currently, the hybrid model is customized towards the experimental double donor-dot device [1]. Due to the code's modular architecture, it will be possible to rapidly analyze donor diffusion and worst case configurations for a large number of different donor cluster geometries. This allows for interesting studies on donor diffusion effects and the statistical distribution of worst case binding energy configurations as a function of donor cluster geometries.

5.2.3 Anticipated Results

This research will enable large-scale statistical analysis of binding energy confidence maps for arbitrary donor cluster geometries, and varying number of donors and electrons. Upon completion, this research will yield the most comprehensive statistical characterization tool for identifying donor numbers in donor clusters with atomic-scale resolution and realistic donor diffusion effects. Further development of our hybrid atomistic/empirical methodology will expand modeling capabilities to allow rapid statistical comparison of different donor cluster geometries and donor diffusion effects.

5.3 Hyperfine Coupling in Multi-Million Configuration Donor-Clusters

5.3.1 Motivation

Scalable donor-based quantum-computing architectures envision arrays of donor spin qubits, in which both single- and two-qubit operations are achieved by independently controlling each qubit using local magnetic [38] and electric fields [39] [1]. High-fidelity selection of individual qubits in qubit arrays, such as through excitation of electron spin resonance (ESR) transitions, is a major challenge. Qubit selectivity can be achieved by tuning a specific qubit's ESR frequencies into resonance with a

globally applied microwave field and by electrical control of the hyperfine coupling between the electron and donor-nuclear spins [38] [40].

5.3.2 Background

Hyperfine coupling describes the interaction of unpaired electrons with nuclear spins. Hyperfine coupling leads to further energy splitting of the electron spin states [14]. The magnitude of the hyperfine coupling induced energy splitting can be tuned with electric fields, and experimentally probed by, for example, energy spin resonance spectroscopy. For quantum computing applications, control and manipulation of hyperfine coupling is seen as a promising path towards accurate accessing of individual qubits in qubit arrays. By applying global microwave fields in conjunction with electrically controlled hyperfine coupling, selective access of qubits through unique ESR frequencies, is envisioned. Selectivity of ESR frequencies can be achieved naturally in donor-based quantum computing, as hyperfine coupling in donor-clusters is very sensitive to the atomic positions and number of donors [38]. The built in selectivity of ESR frequencies in donor-clusters is promising but also challenging to comprehensively predict from a device characterization perspective due to large-scale dopant placement fluctuations and diffusion effects. These inherent statistical donor placement fluctuations in donor-clusters can alter key device metrics and characteristics of future atomic-scale quantum computers considerably [1] [38].

5.3.3 Anticipated Results

We envision modeling of hyperfine coupling in donor-clusters with consideration of large-scale dopant placement fluctuations and donor diffusion effects. Atomistic analysis and empirical model development will enable calculation of hyperfine coupling and ESR frequency confidence bands of multi-million configuration donor clusters with atomic-scale resolution. This research will be provide experimentalists with im-

portant design guidelines towards the goal of high-fidelity qubit selection in large-scale qubit arrays.

5.4 Spin Relaxation in Multi-Million Configuration Donor-Clusters

5.4.1 Motivation

Spin decoherence is an important quality measure for qubits. Long spin relaxation times are important for achieving low-error rates in spin-based quantum computing [41]. The T1 spin-lattice relaxation time is strongly dependent upon the number of donors and donor location. Atomic-scale diffusion of donors further decreases prediction accuracy. Comprehensive device characterization of donor clusters thus necessitates multi-million donor configuration modeling of spin relaxation times.

5.4.2 Background

In order to execute quantum computation algorithms using spin-based qubits, it is necessary to preserve the coherence of the electron spin states for as long as possible [43]. Silicon is a promising material to host spin qubits due to its natural abundance of zero nuclear spin isotopes, leading to long spin decoherence (T2) and spin relaxation (T1) times [38]. For example, in bulk P-doped silicon, T1 spin relaxation times close to one hour (T=1.3K, B=0.35T) have been measured [42]. The T2 spin decoherence time is usually much lower due to additional mechanisms which only affect the spin coherence, but has been reported to exceed seconds in highly purified silicon [29]. In donor-clusters, the spin relaxation time is sensitive to the number and precise atomic locations of the donors. Due to inherent random dopant placement fluctuations, accurate prediction of spin relaxation times is thus difficult using only a small number of possible donor configurations. In addition, donor diffusion effects, which increase the effective spatial dimensions of the donor-clusters, further reduce prediction accuracy.

5.4.3 Anticipated Results

We envision modeling of T1 spin relaxation times in multi-million configuration donor-clusters with consideration of large-scale dopant placement fluctuations and donor diffusion effects. Atomistic analysis and empirical model development will enable large-scale calculation of statistical T1 spin relaxation times confidence bands for varying magnetic fields with atomic-scale resolution. This research will be provide experimentalists with comprehensive design guidelines towards engineering donor-clusters with long spin relaxation times.

5.5 A Modular Empirical/Atomistic High-speed Modeling Tool

5.5.1 Motivation

Key performance indicators of donor-based quantum computing devices such as charge stability diagrams, spin relaxation times and hyperfine coupling strengths are sensitive to the number and exact location of donors. Statistical variations of dopant placement can thus influence device behavior considerably in donor-based quantum computing architectures. The absence of modeling methods capable of simulating dopant placement variations comprehensively with atomic resolution thus poses a significant challenge towards the goal of large-scale donor-based qubit arrays.

5.5.2 Background

As different quantum computing architectures vie for attention from industry, any prospective new technology will have to be upheld to rigorous industry standards and large-scale feasibility studies. Inherent atomic-scale statistical dopant placement variations in the fabrication process can influence device behavior in donor-based devices considerably. For example, key performance indicators of donor-based quantum computing devices such as charge stability diagrams, spin relaxation times and hyperfine coupling strengths are sensitive to the number and exact location of donors.

Understanding statistical dopant placement variations is thus necessary for accurate large-scale device characterization on an atomic scale. Addressing the innovation imperative for novel atomic-scale methods capable of modeling realistic statistical dopant placement variations will close a major gap in large-scale device characterization capabilities for donor-based quantum computing devices. We propose a hybrid empirical/atomistic modeling methodology, which will allow rapid computation of key performance indicators with atomic-scale accuracy. Using a modular development approach, this comprehensive set of hybrid models will be easily expandable. Furthermore, statistical cross-analysis between different modules will provide valuable insight into the inter-relationship of key performance indicators in donor-based quantum computing devices.

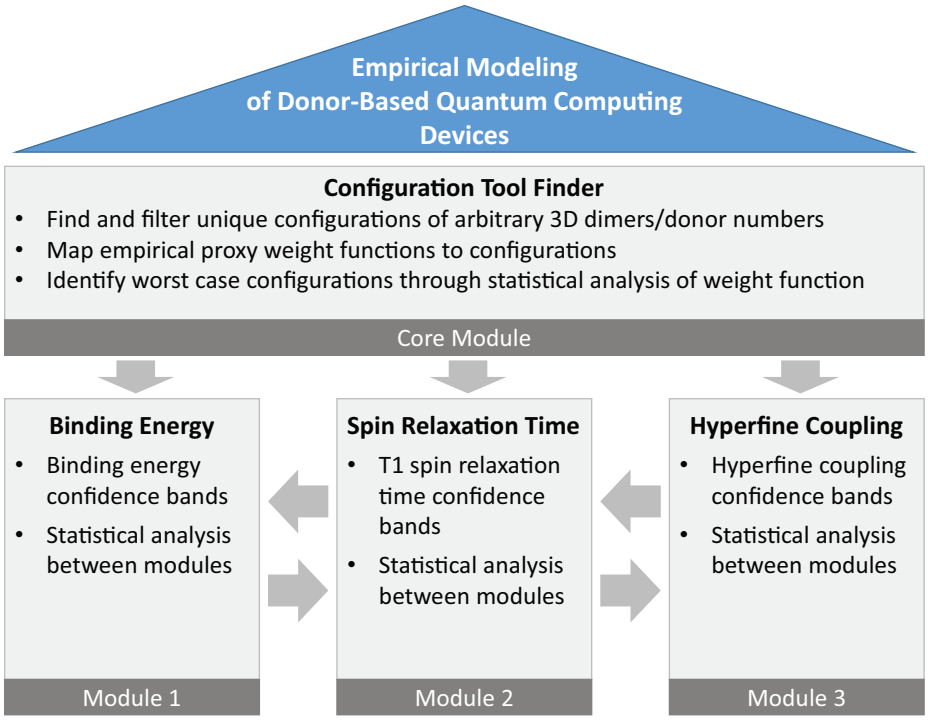

Fig. 5.1. Framework structure of extended hybrid atomistic/empirical modeling methodology for rapid large-scale device characterization of donor-based quantum computing devices.

5.5.3 Anticipated Results

We envision a comprehensive and expandable set of novel hybrid models, which allow high-speed and large-scale statistical device characterization of key performance indicators in donor-based quantum computing architectures. Statistical dopant placement variations and realistic dopant diffusion effects inherent in modern donor-based quantum computing devices will be modeled with atomic-scale accuracy and unprecedented speed using a hybrid empirical/atomistic modeling approach. This research will provide important design guideline implications, and build the modeling capabilities required for future large-scale industry fabrication of donor-based quantum computing devices.

LIST OF REFERENCES

LIST OF REFERENCES

[1] B. Weber, Y. H. M. Tan, S. Mahapatra, T. F. Watson, H. Ryu, R. Rahman, L. C. L. Hollenberg, G. Klimeck, M. Y. Simmons, "Spin blockade and exchange in coulomb-confined silicon double quantum dots" *Nature Nanotechnology*, DOI:10.1038 (2014).

[2] T. Shinada, S. Okamoto, T. Kobayashi, J. R. Barker, and I. Ohdomari, "Enhancing semiconductor device performance using ordered dopant arrays" *Nature*, 437, 1128 (2005).

[3] G. P. Lansbergen, R. Rahman, C. J. Wellard, I. Woo, J. Caro, N. Collaert, S. Biesemans, G. Klimeck, L. C. L. Hollenberg, S. Rogge, "Gate-induced quantum-confinement transition of a single dopant atom in a silicon FinFET" *Nature Physics*, 4, 656-661 (2008).

[4] H. Overhofe, U. Gerstmann, "Ab Initio Calculation of Hyperfine and Superhyperfine Interactions for Shallow Donors in Semiconductors" *Physical Review Letters*, 92, 087602 (2004).

[5] L. C. L. Hollenberg, A. S. Dzurak, C. J. Wellard, A. R. Hamilton, D. J. Reilly, G. J. Milburn, R. G. Clark, "Charge-based quantum computing using single donors in semiconductors" *Phys. Rev. B*, 69, 113301 (2004).

[6] G. Klimeck, S. S. Ahmed, H. Bae, N. Kharche, R. Rahman, S. Clark, B. Haley, S. Lee, M. Naumov, H. Ryu, F. Saied, M. Prada, M. Korkusinski, and T. B. Boykin, "Atomistic Simulation of Realistically Sized Nanodevices Using NEMO 3-DPart I: Models and Benchmarks" *IEEE Trans. Electron Devices*, 54, 9 (2007).

[7] N. Kharche, M. Prada, T. B. Boykin, and G. Klimeck, "Valley splitting in strained silicon quantum wells modeled with 2 degree miscuts, step disorder, and alloy disorder" *Appl. Phys. Lett.*, 90, 9 (2007).

[8] A. Martinez, N. Seoane, A. R. Brown, J. R. Barker, and A. Asenov, *IEEE Trans. Electron Devices*, 8, 5 (2009).

[9] M.Füchsle, J. A. Miwa, S.Mahapatra, H.Ryu, S. Lee, O.Warschkow, L. C. L. Hollenberg, G. Klimeck, M. Y. Simmons, "A single atom transistor", *Nature Nanotechnology*, 7, 242-246 (2012).

[10] G. Klimeck, S. S. Ahmed, H. Bae, N. Kharche, S. Clark, B. Haley. S. Lee, M. Naumov, H.Ryu, F. Saied, M. Prada, M. Korkusinski, T. B. Boykin, R. Rahman, *IEEE Trans. Electron Devices*, 54, 207989 (2007).

[11] G. Klimeck, F. Oyafuso, T. B. Boykin, R. C. Bowen, P. V. Allmen, "Development of a Nanoelectronic 3-D (NEMO 3-D) Simulator for Multimillion Atom Simulations and Its Application to Alloyed Quantum Dots" *Comput. Model.Eng. Sci.*, 3, 60142 (2002).

[12] T. B. Boykin, G. Klimeck,R. C. Bowen, F.Oyafuso, "Diagonal parameter shifts due to nearest-neighbor displacements in empirical tight-binding theory" *Phys. Rev. B*, 66, 125207 (2002).

[13] P. Keating, "Effect of Invariance Requirements on the Elastic Strain Energy of Crystals with Application to the Diamond Structure" *Physical Review*, 145, 637, (1966).

[14] R. Rahman, C. J. Wellard,F. R. Bradbury,M. Prada, J. H. Cole, G. Klimeck, L. C. L. Hollenberg, "High precision quantum control of single donor spins in silicon" *Physical Review Letters*, 99, 036403 (2007).

[15] B. Weber, S. Mahapatra,H. Ryu,S. Lee,A. Fuhrer,T. C. G. Reusch,D. L. Thompson, W. C. T. Lee,G. Klimeck,L. C. L. Hollenberg,M. Y. Simmons, "Ohm's law survives to the atomic scale" *Science*, 335, 6467 (2012).

[16] M. Usman , Y.H.M. Tan, H. Ryu, S. S. Ahmed, H. J. Krenner, T. B. Boykin and G. Klimeck, "Quantitative excited state spectroscopy of a single InGaAs quantum dot molecule through multi-million-atom electronic structure calculations" *Nanotechnology*, 22, 315709 (2011).

[17] N. Kharche, M. Prada, T.B. Boykin, G.Klimeck, "Valley splitting in strained silicon quantum wells modeled with 2 miscuts, step disorder, and alloy disorder" *Appl. Phys. Lett.*, 90, 092109 (2007).

[18] C. W. J. Beenakker, *Physical Review B* "Theory of Coulomb-blockade oscillations in the conductance of a quantum dot", 44, 1646-1656 (1991).

[19] G. Klimeck, R. Lake, S. Datta, "Elastic and inelastic scattering in quantum dots in the Coulomb-blockade regime" *Physical Review B*, 50, 8 (1994).

[20] B. Kane, "A silicon-based nuclear spin quantum computer" *Nature*, 393, 133 (1998).

[21] L. C. L. Hollenberg, A. D. Greentree, A. G. Fowler, and C. J.Wellard, "Two-dimensional architectures for donor-based quantum computing" *Phys. Rev. B*, 74, 045311 (2006).

[22] C. D. Hill, L. C. L. Hollenberg, A. G. Fowler, C. J. Wellard, A. D.Greentree, H. S. Goan, "Global control and fast solid-state donor electron spin quantum computing", *Physical Review B*, 72, 045350 (2005).

[23] L. C. L. Hollenberg, A. S. Dzurak, C. Wellard, A. R. Hamilton, D. J.Reilly, G. J. Milburn, R. G. Clark, "Charge-based quantum computing using single donors in semiconductors", *Physical Review B*, 69, 113301 (2004).

[24] R. Vrijen, E. Yablonovitch, K. Wang, H. W. Jiang, A. Balandin,V. Roychowdhury, T. Mor, D. DiVincenzo, "Electron-spin resonance transistors for quantum computing in silicon-germanium heterostructures", *Physical Review A*, 62, 012306 (2000).

[25] H. Ryu, S. Lee, B. Weber, S. Mahapatra, L. C. L. Hollenberg, M. Y. Simmons, G. Klimeck, "Atomistic modeling of metallic nanowires in silicon" *Nanoscale*, 5, 8666-8674 (2013).

[26] I. Hapke-Wurst, U. Zeitler, H. W. Schumacher, R. J. Haug, K. Pierz, F. J. Ahlers, "Size determination of InAs quantum dots using magneto-tunneling experiments", *Semiconductor, Science and Technology*, 14, L41-L43 (1999).

[27] T. Schmidt, R. J. Haug, K. v. Klitzing, A. Foerster, H. Lueth, "Observation of the local structure of Landau bands in a disordered conductor" *Physical Review Letters*, 8, 78 (1997).

[28] A. Badrutdinov, S. Huang, K. Kono, K. Ono, D. Tayurskii, "Cotunneling effects in GaAs vertical double quantum dots", *JETP Lett.* 93, 199-202 (2011).

[29] A. M. Tyryshkin, S. Tojo., J. J. L. Morton, H. Riemann, N. V. Abrosimov, P. Becker, H.-J. Pohl, T. Schenkel, M. L. W. Thewalt, K. M. Itoh, S. A. Lyon "Electron spin coherence exceeding seconds in high-purity silicon" *Nature Materials* 11, 143-147 (2012).

[30] Morello, A, Pla, J. J., Zwanenburg, F. A.,Chan, K. W.,Tan, K. Y.,Huebl, H.,Mottonen, M., Nugroho, C. D., Yang, Changyi, van Donkelaar, J. A., Alves, A. D. C., Jamieson, D. N., Escott, C. C., Hollenberg, L. C. L., Clark, R. G., Dzurak, A. S. "Single-shot readout of an electron spin in silicon" *Nature* 467, 687-691 (2010).

[31] Pla, J. J., Tan, Kuan Y., Dehollain, Juan P., Lim, Wee H., Morton, John J. L., Jamieson, David N., Dzurak, Andrew S., Morello, A. "A single-atom electron spin qubit in silicon" *Nature* 489, 541-545 (2012).

[32] Koiller, B., Hu, X., and Das Sarma, "Exchange in Silicon-Based Quantum Computer Architecture" *Physical Review Letters* 88, 027903 (2001).

[33] C. J. Wellard, L. C. L. Hollenberg, F. Parisoli, L. M. Kettle, H.-S. Goan, J. A. L. McIntosh, D. N. Jamieson "Electron exchange coupling for single-donor solid-state spin qubits" *Physical Review B* 68, 195209 (2003).

[34] J. R. Petta, A. C. Johnson, J. M. Taylor, E. A. Laird, A. Yacoby, M. D. Lukin, C. M. Marcus, M. P. Hanson, A. C. Gossard "Coherent Manipulation of Coupled Electron Spins in Semiconductor Quantum Dots" *Science* 309, 2180-2184 (2005).

[35] Ono, K., Austing, D. G., Tokura, Y., and Tarucha, S. "Current Rectification by Pauli Exclusion in a Weakly Coupled Double Quantum Dot System" *Science* 297, 1313-1317 (2002).

[36] Johnson, A. C., Petta, J. R., Marcus, C. M., Hanson, M. P., and Gossard, A. C. "Singlet-triplet spin blockade and charge sensing in a few-electron double quantum dot" *Physical Review B* 72, 165308 (2005).

[37] Fang, A., Chang, Y. C., Tucker, J. R. "Effects of J-gate potential and uniform electric field on a coupled donor pair in Si for quantum computing" *Physical Review B* 66, 155331 (2002).

[38] H. Buech, S. Mahapatra, R. Rahman, A. Morello, M. Y. Simmons, "Spin readout and addressability of phosphorus-donor clusters in silicon" *Nature Communications*, DOI: 10.1038 (2013).

[39] B. Weber, S. Mahapatra, T. F. Watson, M. Y. Simmons, "Engineering independent electrostatic control of atomic-scale (4nm) silicon double quantum dots" *Nano Letters*, 12, 4001-2006 (2012).

[40] C. D. Hill, L. C. L. Hollenberg, A. G. Fowler, C. J. Wellard, A. D. Greentree, H. -S Goan, "Global control and fast solid-state donor electron spin quantum computing", *Physical Review B*, 72, 045350 (2005).

[41] W. M. Witzel, M. S. Carroll, A. Morello, L. Cywinski, S. Das Sarma, "Electron Spin Decoherence in Isotope-Enriched Silicon", *Physical Review Letters*, 105, 187602 (2010).

[42] G. Feher, E. A. Gere, "Electron spin resonance experiments on donors in silicon. II. Electron spin relaxation effects", *Physical Review*, 114, 1245-1256 (1959).

[43] L. Chirolli, G. Burkard, "Decoherence in Solid State Qubits", *Advances in Physics*, 57, 3, 225-285 (2008).

[44] N. Shaji, C. B. Simmons, M. Thalakulam, L. J. Klein, H. Qin, H. Luo, D. E. Savage, M. G. Lagally, A. J. Rimberg, R. Joyn, M. Friesen, R. H. Blick, S. N. Coppersmith, M. A. Eriksson, "Spin blockade and lifetime-enhanced transport in a few0electron Si/SiGe double quantum dot", *Nature Physics*, 4, 540-544 (2008).

[45] M. G. Borselli, R. S. Ross, A. A. Kiselev, E. T. Croke, K. S. Holabird, P. W. Deelman, L. D. Warren, I. Alvarado-Rodriguez, I. Milosavljevic, F. C. Ku, W. S. Wong, A. E. Schmitz, M. Sokolich, M. F. Gyure, A. T. Hunter, "Measurement of valley splitting in high-symmetry Si/SiGe quantum dots", *Applied Physics Letters*, 108, 206812 (2012).

[46] B. Roche, E. Dupont-Ferrier, B. Voisin, M. Cobian, X. Jehl, R. Wacquez, M. Vinet, Y.-M. Niquet, M. Sanquer, "Detection of a Large Valley-Orbit Splitting in Silicon with Two-Donor Spectroscopy", *Physical Review Letters*, 108, 206812 (2012).

[47] E. Dupont-Ferrier, B. Roche, B. Voisin, X. Jehl, R. Wacquez, M. Vinet, M. Sanquer, S. De Franceschi, "Coherent Coupling of Two Dopants in a Silicon Nanowire Probed by Landau-Zener Stueckelberg Interferometry", *Physical Review Letters*, 110, 136802 (2013).

[48] O. Warschkow, H. F. Wilson, N. A. Marks, S. R. Schofield, N. J. Smith, P. V. Smith, M. W. Radny, D. R. McKenzie, M. Y. Simmons, "Phosphine adsorption and dissociation on the Si(001) surface: An ab initio survey of structures", *Physical Review B*, 72(12), 125328 (2005).

[49] H. F. Wilson, O. Warschkow, N. A. Marks, N. J. Curson, S. R. Schoeld, T. C. G. Reusch, M. W. Radny, P. V. Smith, D. R. McKenzie, M. Y. Simmons, "Thermal dissociation and desorption of PH_3 on Si(001): A reinterpretation of spectroscopic data", *Physical Review B*, 74, 195310 (2006).

[50] L. Oberbeck, N. J. Curson, T. Hallam, M. Y. Simmons, G. Bilger, R. G. Clark, "Measurement of phosphorus segregation in silicon at the atomic scale using scanning tunneling microscopy", *Applied Physics Letters*, 85, 1359 (2004).

[51] L. Kipp, R. D. Bringans, D. K. Biegelsen, J. E. Northrup, A. Garcia, L.-E. Swartz, "Phosphine adsorption and decomposition on Si(100) 2x1 studied by STM", *Physical Review B*, 52, 5843 (1995).

[52] B. Weber, H. Ryu, Y.-H. M. Tan, G. Klimeck, M. Y. Simmons "Limits to metallic conduction in atomic-scale quasi-one-dimensional silicon wires", *Physical Review Letters*, 113, 246802 (2014).

[53] P. W. Anderson, "Absence of diffusion in certain random lattices", *Phys. Rev*, 109, 1492 (1958)

APPENDICES

A. NATURE NANOTECHNOLOGY SUPPLEMENTARY INFORMATION

Spin Blockade and Exchange in Coulomb-confined Silicon Double Quantum Dots [1]

S1: Determination of the possible donor configurations withing STM patterned dots

First principles based DFT simulations of phosphorus dopant incorporation in silicon using phosphine gas as a dopant precursor [48, 49] have shown that P atoms incorporate at substitutional sites of the silicon lattice. As such within a patch of certain size there are only a limited number of configurations that exist in which the P atoms can occupy substitutional sites relative to each other. To determine the number of all possible configurations that these dopants could occupy after silicon encapsulation (during which time we know there is 1nm diffusion of the donors in the lateral and vertical directions [50]) we have developed a code which calculates the total number of possible donor configurations within the 3D Si crystal. Specifically, the code first matches each possible donor location in the Si crystal, see Figure S1 (a) to a unique identification or tile number, see Figure S1 (b).

For the 0.25ML doping densities used in our devices, P-P dimers are not formed [51] and the nearest position of P donors would be tiles 12-18. As such we can determine all possible permutations of tile numbers depending on the number of donors in the system. The geometric structure information of the dimer is translated into the code through boundary conditions between tiles. Once P-P bonds are filtered out via defined tile occupation rules we determine that there are 30,983 allowed configurations for the 2P case; 2,507,483 for the 3P case and 149,664,630 for the 4P case. Depending on the size of the dot and the number of electrons, the number of possible configurations to calculate binding energies for can exceed many tens of thousands. We thus implement symmetry matching algorithms to segment configurations into

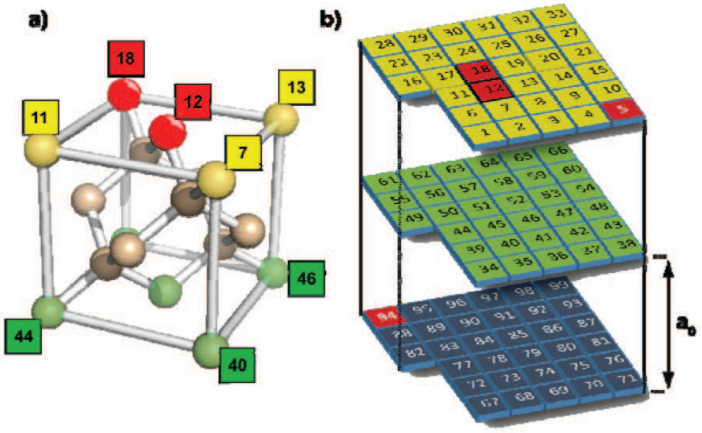

Figure S1: (a) Locations of potential donor sites within a silicon crystal, where a_0 represents the silicon lattice constant. (b) A 3D layer representation of the unit cell sites, where we can determine the minimum distance between P donors (12-18) and the maximum distance assuming ~1nm diffusion in all directions (5-94).

Fig. A.1.

a smaller number of unique configurations with respect to binding energy. If the number of unique configurations is small enough (e.g. 10-100), we can use atomistic tight-binding simulations to firstly calculate the unique 1e binding energies and then extrapolate these results into the entire configuration space.

S2: Empirical Modeling of 1e Binding Energies For large donor numbers (e.g. 3P/4P incl. 3D diffusion), the number of unique configurations is too large for an atomistic tight binding approach. We thus developed an empirical model for predicting 1e binding energies of millions of configurations based on an extensive dataset of atomistically calculated 1e binding energies. We define an inter-donor distance distribution function by summing the distances between donors for each configuration. Specifically, small inter-donor distance distribution function values correspond to close configurations with high binding energies, whereas large inter-donor distance distribution function values describe spread out donor configurations with lower binding energies. This distribution function is strongly correlated to our calculated 1e binding energies, which can be empirically quantified by an inverse power law. Using the configuration finder tool and empirical distribution functions deduced from a limited set of atomistic tight-binding calculations, we are thus able to calculate 1e binding

energies for millions of configurations. Furthermore, analysis of the distribution function allows quick identification of closest and furthest configurations, and helps to classify the configurations into confidence bands.

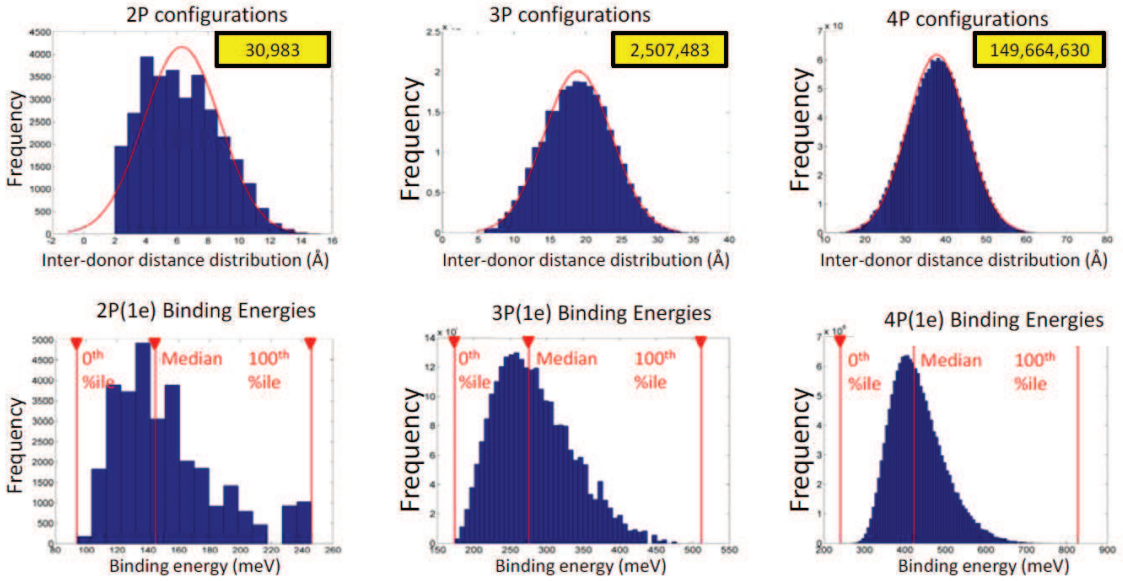

Figure S2: Inter-donor distance distribution functions (in units of a_0=0.38 nm) used to determine the distribution of 1e binding energies for 2P/3P and 4P. The yellow numbers represent the total number of configurations within the dots taking into account dopant diffusion of ≤1nm.

Fig. A.2.

S3: Empirical Modeling of Higher Electron Binding Energies When modelling higher electron binding energies, self-consistent tight-binding calculations take even longer with empirical modelling permitting rapid iterative calculation of binding energiesfor large numbers of configurations. Detailed statistical analysis of our atomistically calculated dataset of higher electron number binding energies confirmed that the relative percentage drop of binding energies with increasing number of electrons is strongly correlated. Specifically, if E_B(N) is the binding energy of the Nth electron for a donor cluster, the percentage change in binding energy between the N+1 and the N-th electron was found to vary linearly with E_B(N) for all N. This enables us to

extrapolate the higher electron binding energies for a large number of cluster configurations by using linear fitting functions. Benchmarking of these empirically deduced fit functions against atomistically calculated binding energies yields high accuracies of ~ 95 percent, confirming the validity of our hybrid modeling approach. By combining the results from steps S1, S2 and S3, we can then calculate and statistically analyze confidence bands composed of millions of configurations, as shown in Figure 3.11

VITA

VITA

Yui-Hong Matthias Tan was born in Bonn, Germany. He is currently a PhD candidate in electrical engineering at Purdue University. His PhD research focuses on silicon quantum electronics and computational nanotechnology. He received his German Dipl.-Ing. engineering degree in electrical engineering from Ruhr University Bochum, Germany in 2010. Matthias worked in management consulting at The Boston Consulting Group in Germany, in semiconductor technology at Intel in Silicon Valley, and in laser optics at the Max-Planck-Institute of Quantum Optics in Germany. He was a PhD fellow of the U.S. National Science Foundation in Australia and South Korea and a fellow of the German National Academic Foundation (Studienstiftung des deutschen Volkes).